

This is the peer reviewed version of the following article:

Finite-element modeling of neuromodulation via controlled delivery of potassium ions using conductive polymer-coated microelectrodes / Verardo, Claudio; Mele, Leandro Julian; Selmi, Luca; Palestri, Pierpaolo. - In: JOURNAL OF NEURAL ENGINEERING. - ISSN 1741-2552. - 21:2(2024), pp. 1-18. [10.1088/1741-2552/ad2581]

Terms of use:

The terms and conditions for the reuse of this version of the manuscript are specified in the publishing policy. For all terms of use and more information see the publisher's website.

26/12/2024 06:33

(Article begins on next page)

Finite-element modeling of neuromodulation via controlled delivery of potassium ions using conductive polymer-coated microelectrodes

Claudio Verardo^{*,1,3}, Leandro Julian Mele^{*,1,4}, Luca Selmi²,
Pierpaolo Palestri^{1,2}

¹ Polytechnic Department of Engineering and Architecture, Università degli Studi di Udine, Udine, Italy

² Department of Engineering “Enzo Ferrari”, Università degli Studi di Modena e Reggio Emilia, Modena, Italy

³ BioRobotics Institute and Department of Excellence in Robotics and AI, Scuola Superiore Sant’Anna, Pisa, Italy

⁴ Department of Materials Science and Engineering, Stanford University, Stanford, United States of America

* The authors contributed equally to the work.

E-mail: pierpaolo.palestri@uniud.it

Abstract. *Objective.* The controlled delivery of potassium is an interesting neuromodulation modality, being potassium ions involved in shaping neuron excitability, synaptic transmission, network synchronization, and playing a key role in pathological conditions like epilepsy and spreading depression. Despite many successful examples of pre-clinical devices able to influence the extracellular potassium concentration, computational frameworks capturing the corresponding impact on neuronal activity are still missing. *Approach.* We present a finite-element model describing a PEDOT:PSS-coated microelectrode (herein, simply *ionic actuator*) able to release potassium and thus modulate the activity of a cortical neuron in an *in-vitro*-like setting. The dynamics of ions in the ionic actuator, the neural membrane, and the cellular fluids are solved self-consistently. *Main results.* We showcase the capability of the model to describe on a physical basis the modulation of the intrinsic excitability of the cell and of the synaptic transmission following the electro-ionic stimulation produced by the actuator. We consider three case studies for the ionic actuator with different levels of selectivity to potassium: ideal selectivity, no selectivity, and selectivity achieved by embedding ionophores in the polymer. *Significance.* This work is the first step toward a comprehensive computational framework aimed to investigate novel neuromodulation devices targeting specific ionic species, as well as to optimize their design and performance, in terms of the induced modulation of neural activity.

1. Introduction

Extracellular potassium is a crucial modulator of neuronal activity [1], [2]. An increase in its concentration $[K^+]$ lowers the outward K^+ fluxes in the ion channels, thereby depolarizing the membrane potential and increasing the intrinsic excitability of the cell [3]. As a result of depolarization, synaptic transmission at excitatory synapses is facilitated, since the postsynaptic current at the glutamatergic receptors is enhanced

38 and the release of neurotransmitters is promoted by a major presynaptic inflow of
 39 calcium through voltage-gated Ca^{2+} channels [4]–[6]. At the network level, potassium
 40 accumulation and diffusion generate non-synaptic coupling between neurons, which
 41 in turn shapes network activity and may induce synchronization [7]. Perturbations
 42 of $[\text{K}^+]$ are interesting also from a neurological perspective, since they are linked to
 43 many pathological conditions such as epilepsy [8], [9] or spreading depression [10], [11].
 44 Therefore, the control of $[\text{K}^+]$, which we will thereafter refer to as *ionic stimulation*, is
 45 drawing attention as a possible innovative pathway toward neuromodulation [12]. This
 46 has been implemented by several novel devices, herein referred to as *ionic actuators*,
 47 capable of perturbing the extracellular concentration of potassium at spatiotemporal
 48 scales approaching those of neuron activity [13]–[15].

49 Ionic stimulation obtained with ionic actuators fits in the broader realm of drug-
 50 delivery devices applied to neuromodulation. A prominent class of such technology relies
 51 on the properties of conductive polymers (CPs) [16], also known as organic mixed ionic
 52 and electronic conductors (OMIECs) [17]. CP-coated electrodes can modulate the local
 53 ionic concentration upon application of an electrical stimulus which translates into the
 54 injection of holes‡ (or electrons) in the polymer backbone and is followed by the release
 55 of pre-charged cations (or anions) in the target electrolyte. The pre-charging can be
 56 achieved using the electrostatic forces provided by fixed moieties in the CP blend or
 57 when the charged drugs act as dopants [18]–[20]. In the purely electrostatic CP loading,
 58 selectivity can be achieved by adding ionophores [21]–[23], using ion-selective membranes
 59 [24] or cell membrane bilayers with specific ion-channel expressions [25]. Alternative
 60 architectures that stem from the field of iontronics [26], bypass the selectivity problem
 61 by employing multiple electrolyte reservoirs where ions/drugs are stored, delivered or
 62 drained [13]–[15]. However, this approach poses evident challenges in the design and
 63 implementation of the microfluidics, requires high voltages and is thus not easy to
 64 miniaturize.

65 Multiphysics computational models are pivotal to aid the design and deployment
 66 of ionic actuators as neuroengineering devices, as they reduce the need for *in-*
 67 *vitro*/animal studies and the prototyping cost and development time. Indeed, they
 68 allow to improve the understanding of the device operation, by providing insight into
 69 underlying phenomena not directly accessible by experiments. Moreover, they enable the
 70 investigation of large regions in the parametric space, paving the way for optimum design
 71 of the neuromodulation devices. Modeling the dynamics of ionic actuators requires an
 72 accurate description of the ions’ electrodiffusion. Given the relatively large dimensions
 73 of these devices, the Poisson-Nernst-Planck (PNP) model [27] is a good candidate to
 74 capture both drift and diffusion transport mechanisms, as well as charge screening effects
 75 in the space-time domain. The PNP model can also be adapted to CPs [28], and has been
 76 employed in computational works focusing on the characterization and optimization of
 77 iontronic devices [29]–[31] or ISM-cuff electrodes [32]. Notwithstanding, to the extent of

‡ More precisely, the injection of holes is associated with the creation of polarons and bipolarons in the polymer. In this paper, we use the term *holes* to ease the discussion.

78 our knowledge, computational frameworks accounting for both ionic actuators and their
79 effect on neuronal membranes are still missing in the literature. This is in contrast with
80 other neuroengineering modalities, e.g., electrical stimulation, where similar modeling
81 frameworks are employed [33], [34].

82 The main difficulty of coupling the description of ionic actuators and neuronal
83 activity resides in the workhorse models employed in computational neuroscience: the
84 volume conductor description of the cellular fluids [35], and the cable theory framework
85 of membrane dynamics [36]. Indeed, the former assumes the neuron milieu to be ohmic,
86 while the latter relies on a circuit-level description of the transmembrane fluxes. As a
87 result, the modeled electric currents have no direct connection with the underlying ionic
88 fluxes. This is not an issue when modeling, e.g., the electric interaction with electrodes
89 for stimulation [33], [34] and recording [37], [38], but becomes pivotal in presence of
90 ionic actuators (see Methods). A small body of literature applied the PNP framework
91 to describe ionic transport phenomena occurring in nervous tissues [39]–[42], mainly
92 focusing on the study of slow potentials and microdomains. We point out that these
93 frameworks exploit the quasistatic approximation of Maxwell equations [35], thereby
94 neglecting capacitive and inductive effects in the cellular fluids. Also, there exists a
95 family of models describing ion dynamics in the nervous milieu under the assumption
96 of only diffusive fluxes [43]–[48]. However, this is in general not justifiable for non-
97 biological electrogenic sources like ionic actuators, since that approach neglects possible
98 components of electric stimulation arising from ion release/uptake.

99 In this work, we propose the first *in-silico* framework that describes the coupled
100 dynamics of a ionic actuator, ion transport in the intra- and extra-cellular fluids (ICF,
101 ECF), and the electrogenic processes at the neural membrane. These models are solved
102 in a self-consistent fashion according to the electrodiffusive level of detail. As a case
103 study, we use a PEDOT:PSS-coated microelectrode releasing K^+ placed below a cortical
104 neuron soma with dome geometry. This configuration enables us to examine how the
105 action of the ionic actuator affects neural activity, both through the perturbation of the
106 extracellular potassium concentration (*ionic stimulation*) and of the electrical potential
107 (*electric stimulation*). First, we showcase the extreme cases of an ionic actuator with
108 either ideal selectivity or no selectivity to K^+ . In the ideal case, the sole action
109 of the ionic actuator is sufficient to drive ionically the neuron into tonic firing or
110 depolarization block. In the non-selective case, mainly electric stimulation is delivered
111 since the polymer is not able to collect enough potassium from the extra-cellular fluid.
112 Second, we study a possible functionalization of the actuator’s selectivity by resorting
113 to ionophores. Simulations show that the optimized ionic actuator enhances the neuron
114 sensitivity to concurrent electrical stimulation as well as to facilitate excitatory synaptic
115 transmission.

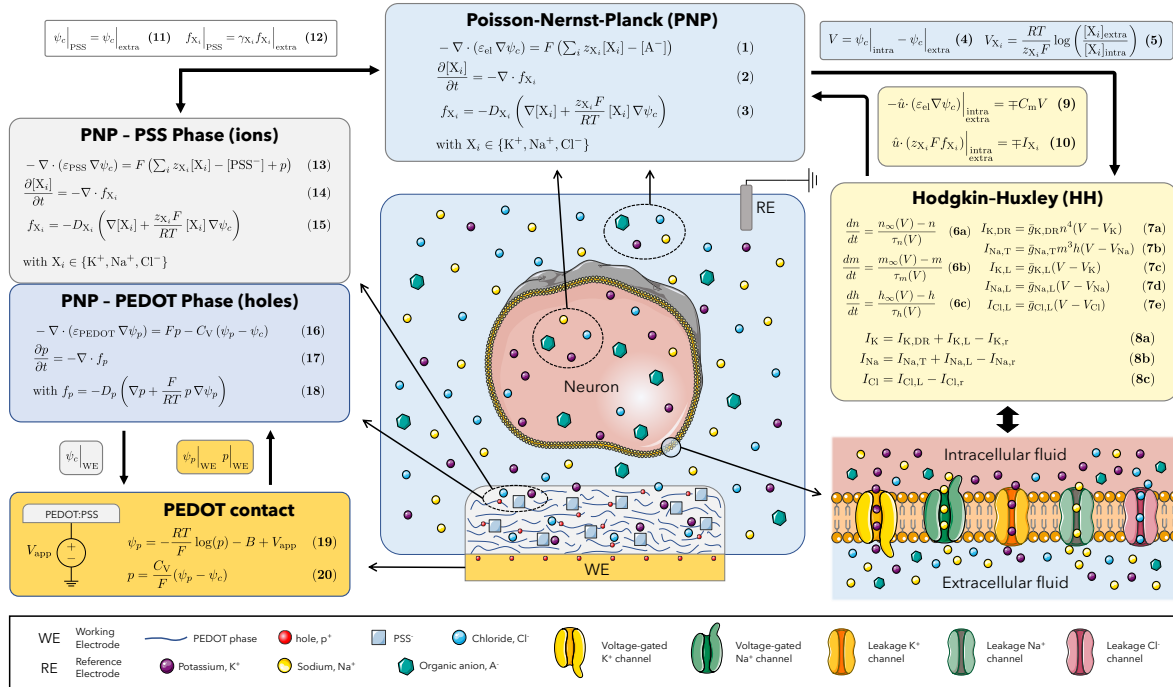


Figure 1. Sketch of the neuron cell (center) containing the intracellular fluid (ICF) and surrounded by the extracellular fluid (ECF), contacted by an external reference electrode (RE). Below the neuron, the CP-based ionic actuator is contacted by a metal (e.g., gold) electrode operating as working electrode (WE). The operation mechanism consists of electronic doping of the PEDOT phase that induces an ion flux pointing outwards from the CP. The equations used for each physics in the simulation domain are represented by frames placed around the main sketch. Frames are connected with arrows that indicate the coupling equations implemented in COMSOL Multiphysics. A description of the physical variables and parameters is reported in Tables S2 and S3, respectively. Part of the image is adapted from Servier Medical Art, © CC BY 3.0.

116 2. Methods

117 The computational framework used in this work (Fig. 1) couples the dynamics
 118 of the ionic actuator, the ICF, the ECF, and the neural membrane. It combines
 119 modeling efforts from the literature separately accounting for the CP-electrolyte
 120 interaction [28], and ion transport in cellular fluids in presence of the neural membrane's
 121 electrogenic activity [39], [43]. The simulation domains with the corresponding physics
 122 are represented by a frame and a set of equations in Fig. 1. Arrows connecting
 123 frames report the equations that couple different domains. Generalizations of the
 124 computational framework to account for ionophores and synapses are shown in Fig. 2.
 125 A description of the abbreviations, physical variables, and parameters used is reported
 126 in the supplementary materials in Tables S1, S2, and S3, respectively. The model
 127 is implemented in COMSOL Multiphysics [49] (technical details are reported in the
 128 Supplementary Note 1). In the following, we briefly describe the model equations, the
 129 reference physical and geometrical parameters, as well as the case studies examined.
 130 The model verification is addressed in the Supplementary Note 2.

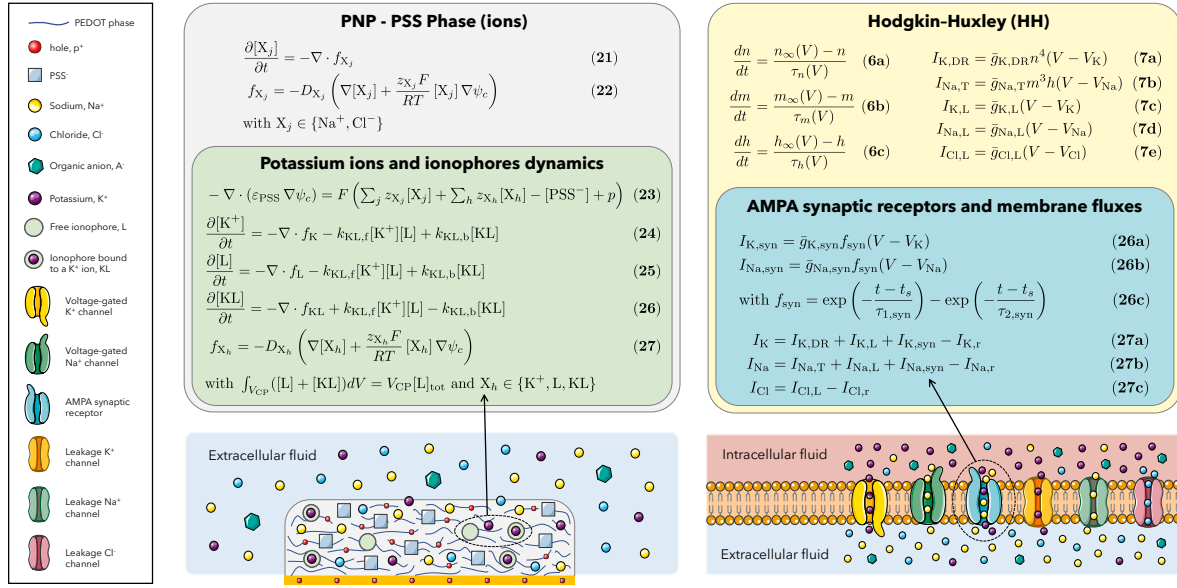


Figure 2. Sketch illustrating the changes made to the modeling framework shown in Fig. 1 to account for the dynamics of ionophores (left) and AMPA excitatory synapses (right). Green and blue insets highlight the new or updated equations in the PNP-PSS model of the CP (grey frame, as in Fig. 1) and the HH model of the neural membrane (yellow frame, as in Fig. 1). A description of the physical variables and parameters is reported in Tables S2 and S3, respectively. Part of the image is adapted from Servier Medical Art, © CC BY 3.0.

131 2.1. Model equations

132 **2.1.1. Intra- and extra-cellular fluids** The ECF and ICF are modeled as electrolytes
 133 using the PNP equations (Eqs. 1-3). The electrostatic potential of the ions, ψ_c , is
 134 obtained by solving the Poisson equation (Eq. 1), which depends on the local space and
 135 time-dependent net charge density due to all the ionic species in the aqueous phase. For
 136 simplicity, we restrict the analysis to the main ionic agents responsible for the generation
 137 of action potentials (APs) at the neural membrane, namely K^+ , Na^+ , Cl^- . The bulk
 138 concentrations are taken from [43], in agreement with typical (artificial) cerebrospinal
 139 fluids [1]. A generic anion A^- , assumed fixed and uniformly distributed for simplicity,
 140 is added to provide electroneutrality (i.e., $[K^+] + [Na^+] - [Cl^-] - [A^-] = 0$) in the bulk of
 141 the solutions. Mass conservation of each mobile species is enforced with the continuity
 142 equations (Eqs. 2). Therefore, time-dependent variations of ionic concentrations are
 143 given by drift and diffusion fluxes and described using the Nernst-Planck transport
 144 equations (Eqs. 3). Note that, Eqs. 1-3 are solved in both the extra and intracellular
 145 domains. The presence of an extracellular reference electrode (RE) is mimicked through
 146 boundary conditions in the ECF's bulk that set the electric potential to ground and the
 147 ionic concentrations to their baseline values. Since no limit on the RE's current is
 148 imposed, such boundary conditions also account for the action of a counter electrode
 149 (CE).

150 *2.1.2. Neural membrane* The transmembrane fluxes through ion channels are modeled
 151 using the Hodgkin-Huxley (HH) formalism (Eqs. 6-8), implemented at each mesh point
 152 of the cell membrane. The HH model of this work has been introduced in [43] and
 153 later used to describe an interneuron of the rat CA1 hippocampus [50], [51]. It includes
 154 a transient sodium current (subscript T) and a delayed rectifying potassium current
 155 (subscript DR), which are voltage-gated and responsible for the generation of APs (Eqs.
 156 7a-b). Moreover, our implementation has a leakage current (subscript L) specific for each
 157 ion species (Eqs. 7c-e), differently to the original HH model [52]. Equation 6 collects
 158 three first-order differential equations modeling the dynamics of the gating variables
 159 for the potassium (n) and sodium (m , h) voltage-gated channels, which depend on the
 160 (in)activation curves n_∞ , m_∞ , h_∞ , and time constants τ_n , τ_m , τ_h , respectively. Equation
 161 8 reports the total transmembrane current density for each ion species, which depends
 162 (through Eq. 7) on the maximum conductances of the ion channels, the gating variables,
 163 and the difference between the membrane and reversal potentials (see Section 2.1.3). In
 164 order to preserve the rest potential V_r of the chosen HH model at the steady state, each
 165 current density in Eq. 8 is shifted by its value $I_{X_i,r}$ at V_r , where $X_i \in \{K^+, Na^+, Cl^-\}$,
 166 and therefore is null under steady-state conditions. We note that alternative choices for
 167 the steady state are possible. For instance, in [39] the authors block the voltage-gated
 168 channels and let the system achieve the thermodynamic equilibrium. Nevertheless, since
 169 sub-threshold fluxes are orders of magnitude smaller than the ones that shape neural
 170 firing, these choices are expected to mildly impact the system’s behavior. Since our
 171 investigations focus on temporal scales of tens to hundreds of milliseconds (see Results),
 172 we do not account for homeostatic mechanisms responsible for the regulation of ion
 173 concentration, such as ion transporters at the neural membrane or spatial buffering by
 174 glial cells [2]. The interaction of these mechanisms with ion dynamics is expected to
 175 become relevant at the scale of seconds or longer [43]–[48].

176 *2.1.3. Coupling HH and PNP models* The currents through ion channels are imposed
 177 as flux boundary conditions in and out of the cell (Eq. 10), according to the ion currents
 178 given by Eq. 8. The dielectric effects of the membrane are modeled as an ideal capacitor
 179 with parallel plates via a thin layer approximation. Namely, they are accounted for
 180 through boundary conditions on the electric displacement field that depends on the
 181 membrane capacitance C_m and the membrane potential V (Eq. 9). These conditions
 182 are responsible for the electrical double layer (EDL) formation at the two sides of the
 183 membrane, and avoid the need to explicitly solve the Poisson equation in the membrane
 184 domain (as done, e.g., in [39]), thereby reducing the computational cost. The HH model
 185 extracts the membrane potential V by sampling the electrostatic potential predicted by
 186 the PNP at the intra- and extra-cellular side of the neural membrane (Eq. 4). Differently
 187 from previous works [39], the runtime calculation of the reversal potentials V_K , V_{Na} , V_{Cl}
 188 is done by sampling the ionic concentrations at a distance $d_s = 6$ nm from the neural
 189 membrane, i.e., a distance 5 times larger than the Debye length [27] in the ECF and ICF
 190 (Eq. 5). This strategy is adopted to avoid distortion of the ion concentrations induced

191 by charge screening effects in the EDL.

192 *2.1.4. Ionic actuator* The ionic actuator consists of a film of conjugated polymer-
 193 polyelectrolyte blend (hereafter simply referred to conductive polymer, CP), that is, a
 194 two-phase domain where both ionic and electronic transport take place simultaneously
 195 (see Fig. 1). We consider a PEDOT:PSS blend as the reference CP and use the model
 196 proposed in [28]. According to [28], the polyelectrolyte PSS phase and the PEDOT
 197 phase can be modeled by coupling two PNP sets of equations: in the PNP of the PSS
 198 phase, the concentration of holes is added to the space charge density of the Poisson
 199 equation so that ions are electrostatically influenced by the holes' spatial distribution
 200 (see Eq. 13); differently, in the PNP of the PEDOT phase the electrostatic potential of
 201 holes, ψ_p , in the Poisson equation (Eq. 16) depends on ψ_c in the form of a capacitive
 202 coupling, namely, through the volumetric capacitance C_V (with units of F/cm³). This
 203 phenomenological term quantifies the extent of entanglement between the two phases
 204 and can be seen as the result of a three-dimensional EDL [53], [54]. Mass conservation of
 205 ions and holes in their respective phase is also ensured by the continuity equations (Eqs.
 206 14 and 17), where electrodiffusive fluxes are described with the Nernst-Planck equation
 207 (Eqs. 15 and 18). Note that, for the sake of simplicity, we do neglect reactions occurring
 208 at the CP/electrolyte interface [55], such as oxygen reduction reactions (ORRs) often
 209 seen in PEDOT:PSS CPs [56]. This phenomenon should translate into an additional
 210 faradaic current drawn by the WE when using a negative bias but should not sensibly
 211 impact the capacitive mechanism that enables the ionic injection in the extracellular
 212 fluid.

213 *2.1.5. Coupling between polyelectrolyte and extracellular fluid* Since polyelectrolyte and
 214 electrolyte phases are both ionic phases, the PSS/ECF interface must ensure continuity
 215 of the electrostatic potential (see Eq. 11). Fluxes of ions, however, may experience
 216 affinity changes due to, e.g., ionophores incorporated in CP [21], [22] or from ion-
 217 selective barriers [25]. For the sake of generality, we equipped our model with virtual
 218 affinity coefficients γ_K , γ_{Na} , γ_{Cl} at the PSS/ECF interface equal to either 0 or 1 (see
 219 Eq. 12) to introduce ideal selectivity of the CP to specific ions (see Section 2.2).

220 *2.1.6. Ionophores* While the parameters γ_{X_i} , $X_i \in \{K^+, Na^+, Cl^-\}$, are used as
 221 phenomenological terms to induce ideal selectivity, ionophores are employed as a more
 222 realistic way to describe a selective ionic actuator [21], [22]. With respect to the ideal
 223 CP, the physics of an ionophore-containing CP (described in Fig. 2, left panel) also
 224 includes the continuity equations (Eqs. 25, 26) for the free ionophores, L, as well as the
 225 selective complexes formed with potassium ions, KL. Forward and backward reaction
 226 terms are included in these equations and the continuity equation for K⁺ ions (Eq. 24)
 227 to account for the binding and unbinding mechanisms of ionophores and potassium ions
 228 [57]. Electrodiffusive fluxes are described by the Nernst-Planck equation (Eq. 27). Note
 229 that ionophores are confined in the CP domain and can be regarded as fixed or mobile

230 depending on the value of their diffusivity coefficient. Moreover, in this work we assume
 231 the ionophore molecules as neutral species so that only their complexed form (positively
 232 charged) contributes to the Poisson equation (Eq. 23). The continuity equations and the
 233 electrodiffusive fluxes for Na^+ and Cl^- are the same as in Eqs. 14-15 but, for the sake
 234 of clarity, they are also reported in Eqs. 21-22 to explicitly separate the K^+ dynamics.

235 *2.1.7. Synapses* A model of excitatory synapse (described in Fig. 2, right panel) is
 236 included in the neural membrane when testing the neuromodulation capability of the
 237 CP beyond to purely induce APs (see Section 3.4). The model is taken from [58] and
 238 accounts for the K^+ and Na^+ fluxes through an AMPA postsynaptic receptor (Eq.
 239 26). We consider only single synaptic events for each simulation. The excitatory
 240 postsynaptic currents (EPSCs) are described with a template profile for the ion
 241 postsynaptic conductances, and are modulated by the membrane and reversal potentials.
 242 The total transmembrane currents for each ion species are updated accordingly (Eq.
 243 27). Differently to [58], we neglect the small calcium component to avoid the additional
 244 computational cost of modeling the Ca^{2+} electrodiffusion in the cellular fluids.

245 *2.2. Case studies for the ionic actuator*

246 In the present work, we consider 3 case studies of CP with different levels of selectivity
 247 towards K^+ in terms of storage and release.

- 248 • *Ideally-selective CP* (isCP): Na^+ ions cannot enter the CP. This is accomplished by
 249 setting $\gamma_{\text{Na}} = 0$ while $\gamma_{\text{K}} = \gamma_{\text{Cl}} = 1$. The physical parameters of the CP are taken from
 250 the literature [28], [53], [55] and ionophores are not embedded in the CP backbone.
 251 As a result, the CP in the undoped state is pre-charged almost completely with
 252 K^+ , which compensates the fixed moieties PSS^- .
- 253 • *Non-selective CP* (nsCP): the CP is permeable to all of the ions ($\gamma_{\text{Na}} = \gamma_{\text{K}} = \gamma_{\text{Cl}} = 1$).
 254 The physical parameters of the CP are taken from the literature [28], [53], [55] and
 255 ionophores are not embedded in the CP backbone. As a result, the CP in the
 256 undoped state is pre-charged by both K^+ and Na^+ , in same proportions as in the
 257 ECF (where $[\text{Na}^+] \gg [\text{K}^+]$).
- 258 • *Ionophores-induced selective CP* (ionoCP): the CP is permeable to all of the ions as
 259 in the previous case, but it is endowed with ionophores, that enhance the proportion
 260 of K^+ ions inside the CP. However, their binding affinity resists to the ion release
 261 into the ECF. To get the best from this trade-off, we tailor the chemical parameters
 262 of the CP and of the ionophores by resorting to a simplified phase boundary model
 263 for the CP with ionophores and its interaction with the ECF (see Supplementary
 264 Note 3).

265 If not otherwise specified, we use the values reported in Table S3 for the physical
 266 parameters. For the convenience of the reader, we report in Table S4 the parameters and
 267 the correspondent values adopted to instantiate the isCP, nsCP, ionoCP case studies.

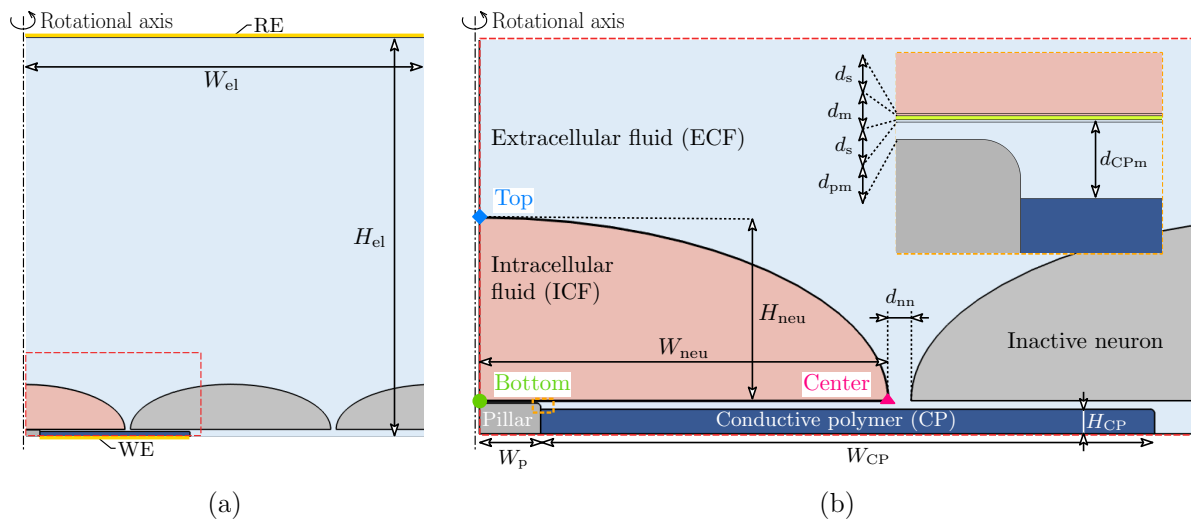


Figure 3. (a) Section of the 2D-axisymmetric geometry used in this work. The active neuron is shown in pink and the CP in blue. Domains in grey are considered inactive and are not included in the simulation space. Metal contacts (WE and RE) with applied potentials are shown by thick yellow lines. (b) Zoom of the active neuron domain, highlighting some relevant points at the neuron membrane: “Top” (blue), “Center” (red), and “Bottom” (green) that will be employed in the figures in the Results section. Orange dashed lines (inset) report an additional zoom of the CP-Neuronal cleft. Additional description of the geometrical parameters and their reference values are reported in Table S5.

268 2.3. Geometry

269 The proposed modeling approach allows us to spatio-temporally resolve ionic gradients
 270 and potential drops in the continuous space including the double layer charge at the
 271 interfaces. As such, this model demands for a refined space discretization capable to
 272 reproduce sub-nanometer features. To reduce computational cost we consider a 2D-
 273 axisymmetric geometrical domain that cuts down the model complexity to the one of
 274 a 2D model but restricts geometry to axial symmetry [59]. The reference simulation
 275 structure used in this work is shown in Fig. 3.a. It includes an active neuron cell (light
 276 red) shaped as a halved oblate ellipsoid (dome) laying on a ring-shaped ionic actuator
 277 (dark blue) immersed in an electrolyte bath (light blue). Lateral neurons (grey, on the
 278 right) are non-active and are included by means of encumbrance to resemble realistic
 279 neighboring cells in a cultured setting. Obviously, their dome shape cannot be enforced
 280 in the 2D-axisymmetrical model so they are essentially rings limiting the ion transport
 281 in the vertical direction as in a realistic culture. An oxide pillar (grey, on the bottom
 282 left) is included to keep the neuron at a given distance from the polymer, leaving an
 283 electrolyte cleft between the two. A zoom-in view of the active neuron boundaries is
 284 reported in Fig. 3.b. If not otherwise specified, we use the values in Table S5 for the
 285 geometrical parameters.

3. Results

3.1. Ideally-selective CP (isCP)

Figure 4 shows the working principle of ion actuation in the isCP case study. Initially, the ionic actuator is biased at a negative potential (dedoped state), $V_{\text{app}} = -1$ V, which corresponds to a very small hole concentration, p , in the CP so that the PSS^- charges are mostly compensated by the stored K^+ ions. By ramping the applied potential, holes are injected into the film (or, in other words, electrons are transferred from the PEDOT into the metal contact) and potassium ions are released in the ECF producing a constant ionic current in accordance with the volumetric capacitive behavior of the CP. The cations diffuse towards the neuron and increase the local extracellular concentration, $[\text{K}^+]$, in the proximity of the cell membrane resulting in membrane depolarization. As shown in Fig. 4.a, a $V_{\text{app,max}} = -0.65$ V produces $\Delta[\text{K}^+] = 20$ mM and is able to induce an *ionic* AP. By increasing the maximum value of the applied voltage, one can further increase the released dose of K^+ and hence the local $[\text{K}^+]$, thereby eliciting multiple APs. An example is shown in Fig. 4.b, where $V_{\text{app,max}} = -0.5$ V induces two consecutive ionic APs. The ionic flux emitted by the CP during the release is proportional to the slope of the ramp stimulus $V_{\text{app}}(t)$, namely $v = dV_{\text{app}}(t)/dt$. Therefore, higher v yields larger transient perturbations of the local concentration of K^+ . This is shown in Fig. 4.c, where the neuron reaches a configuration of depolarization block [60] due to the large perturbation of $[\text{K}^+]$. One should note that, since the CP is assumed perfectly selective to K^+ ions ($\gamma_{\text{Na}^+} = 0$), the increase of $[\text{K}^+]$ induced by the ionic actuator produces a decrease of $[\text{Na}^+]$ and an increase of $[\text{Cl}^-]$ (not shown), owing to electroneutrality. While changes in sodium concentration also contribute to membrane depolarization, their effect is quite limited compared to potassium. This is highlighted in Fig. S1, where we show the reversal potentials as a function of the changes in the extracellular ion concentration. We remark that the initial value of the applied potential $V_{\text{app}} = -1$ V to keep the polymer in a dedoped state depends on the choice of the CP (PEDOT-PSS), the metal contact, and the reference electrode. Therefore, it may vary with different instances of model parameters. Given the purely capacitive nature of CPs assumed in this work, and since we do not model redox reactions between the polymer and the extracellular fluid, no current flows from the WE to RE under constant applied potential.

We point out that, during K^+ release, the bottom side of the neuron is hyperpolarized, while the upper one is depolarized (see the last row in Fig. 4); and the extent of such perturbations is enhanced by larger v . This is due to the drift component of the ionic flux released by the CP, which acts as anodal source of electrical stimulation [61]. Incidentally, this may raise the question that the electrical component may be the main neuromodulation drive of the firing patterns observed in Fig. 4. To rule out this hypothesis, we repeated the same simulations while keeping the reversal potentials fixed to their baseline values (see Fig. S2). Since no APs are elicited in this case, we can confirm that the ionic neuromodulation, and thus the release of potassium ions, is responsible for the neural activity observed in Fig. 4. Fig. S2 also suggests

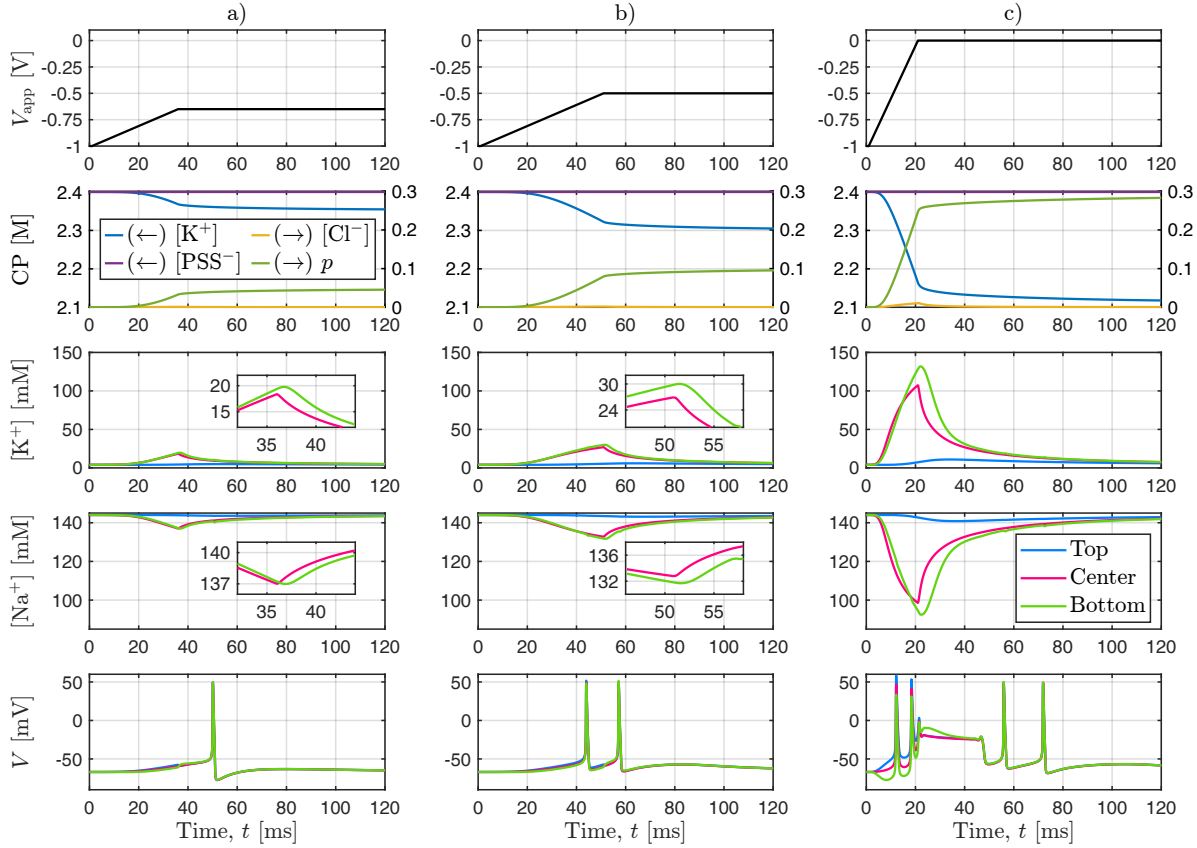


Figure 4. Ideally-selective CP (isCP): examples of ionic neuromodulation transients. Different profiles for the applied potential to the CP are considered: a) $V_{\text{app,max}} = -0.65$ V, $v = 10$ V/s, b) $V_{\text{app,max}} = -0.5$ V, $v = 10$ V/s, c) $V_{\text{app,max}} = 0$ V, $v = 50$ V/s. The rows show, in order: 1) the potential applied to the metal contact below the CP, 2) the concentrations of ions and holes inside the CP, the extracellular concentrations for 3) K^+ and 4) Na^+ , and 5) the membrane potential. The labels “top”, “center” and “bottom” refer to the points marked in Fig. 3.b. In the second row, two different scales are adopted for $[\text{K}^+]$, $[\text{PSS}^-]$ and $[\text{Cl}^-]$, p , respectively (see arrows in the legend).

327 that the slope of the actuation potential must be small enough to limit the electric field
 328 generated by the ionic actuator and therefore ensure a ionic-only stimulation. We point
 329 out that, owing to the capacitive nature of the CP, the currents delivered through ramp
 330 profiles of $V_{\text{app}}(t)$ resemble pulse-shaped waveforms typically used in neuroengineering
 331 devices for electrical stimulation [62], [63].

332 Figure 5 reports different snapshots of the 2D-axisymmetric spatial distributions
 333 of ionic concentrations and potentials of the transient in Fig. 4.a. Three time points
 334 are considered: (left) at the end of K^+ release ($t = 35$ ms), (middle) at the peak of the
 335 elicited AP ($t = 46.87$ ms), and (right) during the post-AP re-equilibration of ions in the
 336 ECF ($t = 80$ ms). A close inspection of the extracellular potential (fourth row) confirms
 337 a non-negligible electrical gradient during release (e.g., the total potential drop in the
 338 neuron-CP cleft is a few mV at $t = 35$ ms), which is responsible for the aforementioned
 339 electric component of neurostimulation.

340 The ion-release performance of the ionic actuator depends on both CP properties

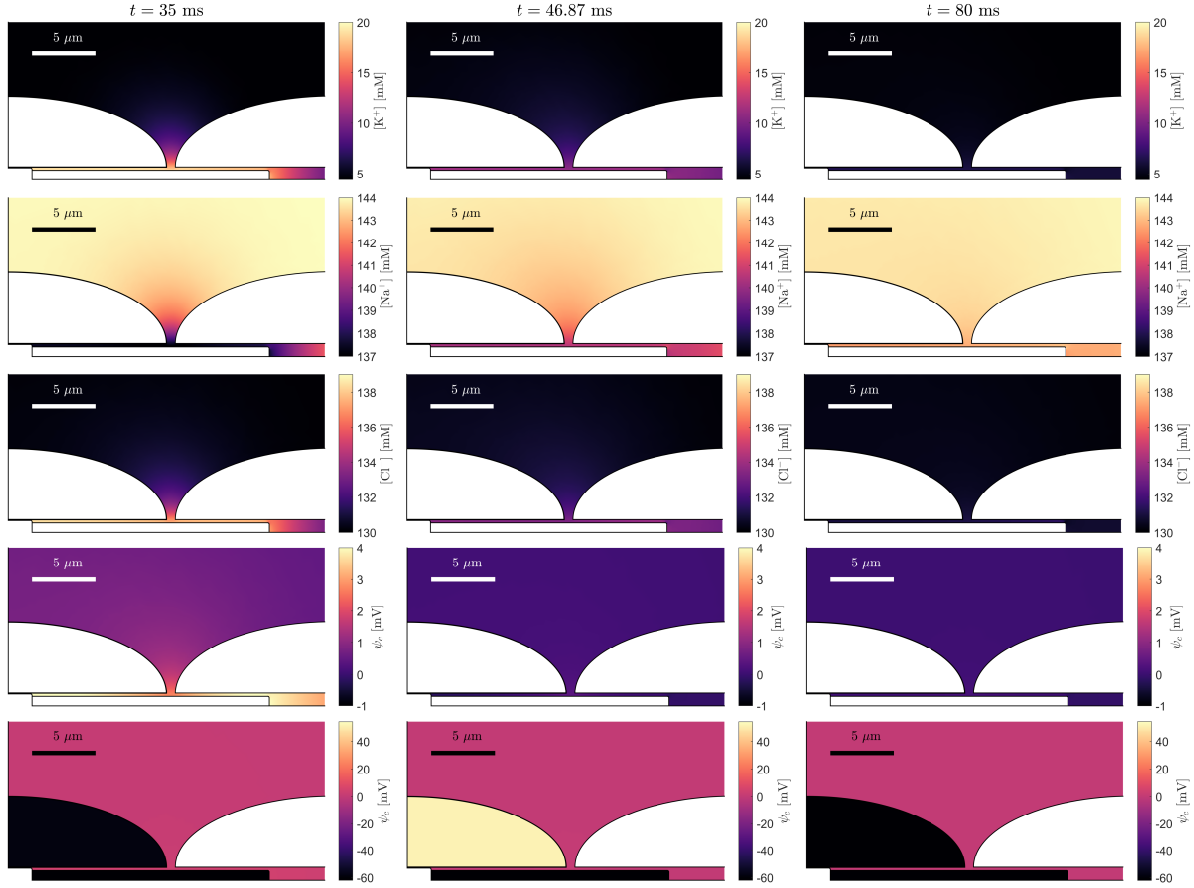


Figure 5. Ideally-selective CP (isCP): 2D-axisymmetric cutplanes illustrating the spatial distributions of different physical variables taken during the transient simulation in Fig. 4.a. Three time snapshots are considered: (left) at the end of K^+ release ($t = 35$ ms), (middle) at the peak of the AP ($t = 46.87$ ms), and (right) during the post-AP re-equilibration of ions in the ECF ($t = 80$ ms). The rows show, in order: the extracellular concentrations of 1) K^+ , 2) Na^+ , and 3) Cl^- , the electric potential 4) in the ECF only and 5) in both the ICF and ECF. Note the different color scale in rows 4) and 5).

341 and geometrical factors. In fact, on one side the available ionic dose is strictly related to
 342 the number of fixed charges incorporated in the film. For example, Fig. S3 shows that
 343 the maximum releasable dose of K^+ decreases with decreasing $[PSS^-]$ in the CP. Once
 344 the CP is depleted from cations, Cl^- anions start entering the CP to balance the excess
 345 holes injected by the metal contact. On the other side, the encumbered space around
 346 CP helps to maintain the perturbation of $[K^+]$ in the bottom part of the neuron for
 347 longer times, thus facilitating ionic APs. This is shown in Fig. S4 where, for the same
 348 V_{app} profile, the change in extracellular $[K^+]$ decreases for larger gaps between the active
 349 and lateral neurons (i.e., low surface density of neurons). A similar effect is obtained
 350 for larger clefts between the neuron and the CP, as illustrated in Fig. S5.

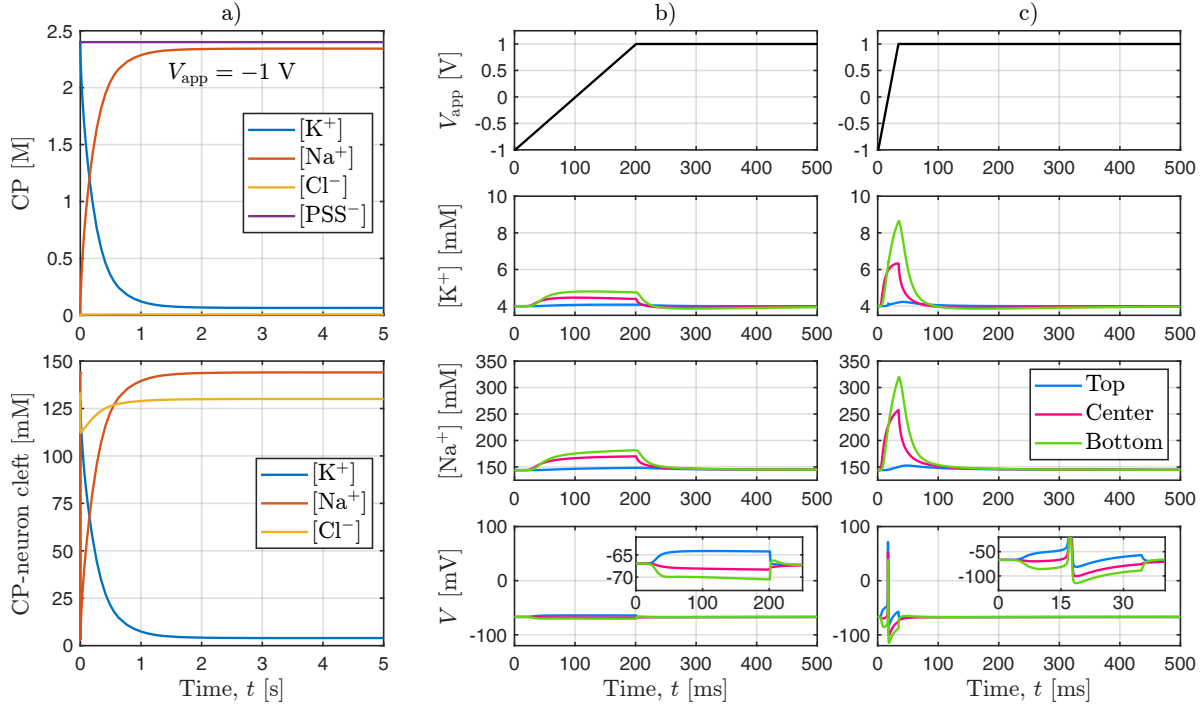


Figure 6. Non-selective CP (nsCP). a) Ion-retention study of the K^+ -preconditioned CP immersed into a physiological fluid while biased at $V_{app} = -1$ V. The top figure shows the time-evolution of the ion concentrations inside the CP, while in the bottom the ones in the CP-neuron cleft. b-c) Examples of ionic neuromodulation transients performed immediately after the ion-retention study. Different slopes for the applied potential are considered (with $V_{app,max} = 1$ V): a) $v = 10$ V/s and b) $v = 60$ V/s. The rows show, in order: 1) the potential applied to the CP, the extracellular concentrations for 2) K^+ and 3) Na^+ , and 4) the membrane potential.

351 3.2. Non-selective CP (nsCP)

352 Figure 6 illustrates the working principle of ion actuation in the nsCP case study.
 353 Since no selectivity to K^+ is enforced, we first tested the CP capability of maintaining
 354 a pre-charged dose of K^+ ions, i.e., we assume that the polymer has been initially
 355 preconditioned with pure KCl that is then replaced with the extracellular fluid. In Fig.
 356 6.a we report the simulation results of such ion-retention study, starting from a CP
 357 pre-charged with K^+ and held in the undoped state ($V_{app} = -1$ V). Being permeable
 358 also to Na^+ , the CP rapidly evolves to a configuration of thermodynamic equilibrium
 359 where K^+ and Na^+ concentrations retain the same ratio as in the ECF, corresponding
 360 to $[K^+]_{CP} = 65.1$ mM, $[Na^+]_{CP} = 2.34$ M, and so $[K^+]_{CP}/[Na^+]_{CP} = 2.8\%$. Therefore, the
 361 CP fails to maintain most of the pre-charged K^+ dose, which is released in the ECF in
 362 an uncontrolled fashion. Compared to the isCP, the available potassium in the nsCP
 363 case is hence reduced by a remarkable factor (37 in our case).

364 Starting from the condition resulting from the transient in Fig. 6.a, we simulate two
 365 examples of ionic actuation with applied stimulus featuring either $v = 10$ V/s or $v = 60$
 366 V/s (Fig. 6.b and c, respectively). Differently to the isCP case, the injection of holes
 367 induces a release of both K^+ and Na^+ ions. Since Na^+ is the dominant ion in the CP,

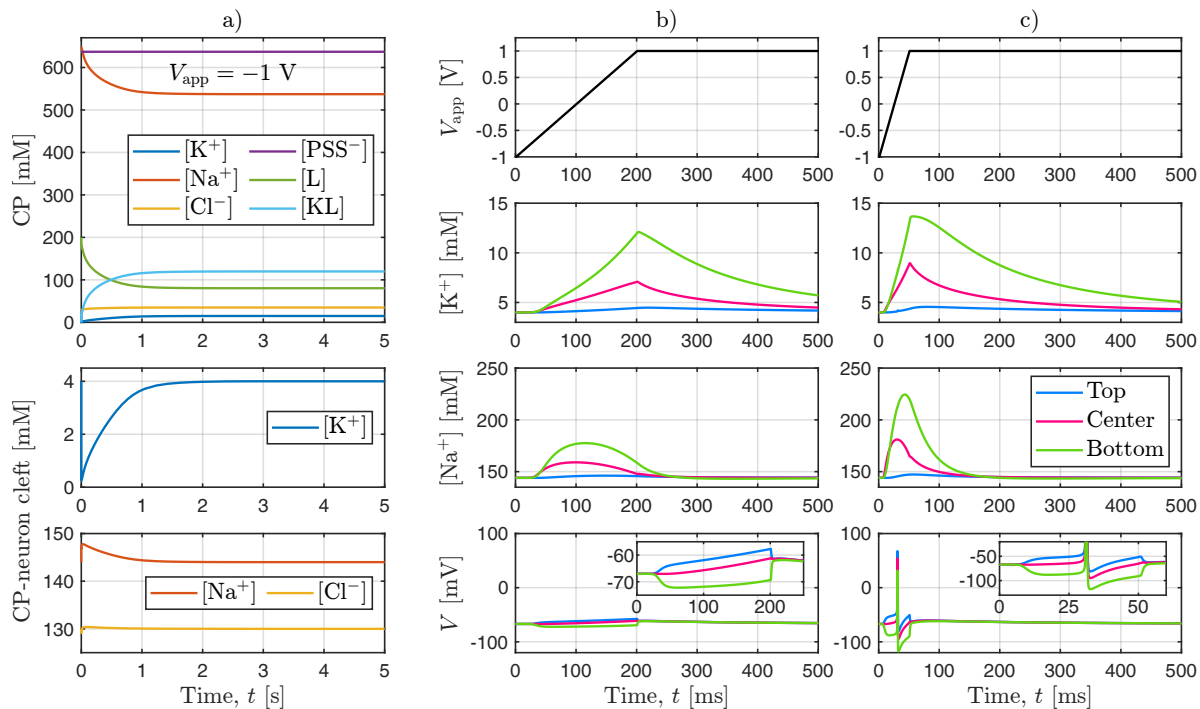


Figure 7. Ionophores-induced selective CP (ionoCP). a) Re-equilibration study with CP biased at $V_{\text{app}} = -1$ V to allow the formation of KL complexes. The first row shows the ion concentrations inside the CP, while the second and third rows the ones in the cleft between the neuron and the CP. b-c) Examples of ionic neuromodulation transients after the re-equilibration study. Different slopes for the applied potential are considered (with $V_{\text{app,max}} = 1$ V): b) $v = 10$ V/s and c) $v = 40$ V/s. The rows show, in order: 1) the potential applied to the CP, the extracellular concentrations for 2) K^+ and 3) Na^+ , and 4) the membrane potential.

368 the ion release predominantly affects the local concentration of sodium ions in the ECF.
 369 In contrast to what we observed in Fig. 4 for the isCP, $[\text{K}^+]$ here increases locally by
 370 only a few mM, despite having applied a larger stimulus, $V_{\text{app,max}} = 1$ V versus $-0.65/-0.5$
 371 V in Fig. 4. Another important finding is that the membrane potential induced by the
 372 nsCP is mostly due to the electric field produced by the applied potential rather than
 373 by the perturbation of the ionic concentrations (mostly $[\text{Na}^+]$). As shown in Fig. 6.c,
 374 an AP can eventually be elicited if v is increased to, e.g., $v = 60$ V/s. However, the AP
 375 persists with an almost identical time course even when the reversal potentials of the
 376 neuron are kept fixed to their baseline values (see Fig. S6). We will thereafter refer to
 377 this kind of stimulation of action potentials as *electric*, i.e., APs not directly induced by
 378 the perturbation of the extracellular ionic concentrations.

379 3.3. Ionophores-induced selective CP (ionoCP)

380 We chose the ionoCP properties according to optimality criteria based on simulations
 381 employing a reduced model of the CP/ECF interaction (see Supplementary Note 3).
 382 The optimization parameters were the equilibrium constant of ionophores β_{KL} and the
 383 concentration of fixed charges in the polymer $[\text{PSS}^-]$. The backward rate constant was

384 set based on the literature ($k_{\text{KL},b} = 10^{-4}$ 1/s as in [64]), while the forward one is by
 385 definition $k_{\text{KL},f} = k_{\text{KL},b} \cdot \beta_{\text{KL}}$. The optimum was evaluated adopting as figure of merit
 386 the $[\text{K}^+]$ change achieved in the finite-volume ECF at steady state (representative of
 387 the ionic stimulation achievable by the ionoCP), for a given applied $V_{\text{app,max}}$. Fig.
 388 S7.a-c show $[\text{K}^+]$ vs $[\text{PSS}^-]$ curves that were obtained for different total concentrations
 389 of ionophore in the system, $[\text{L}]_{\text{tot}}$, and $V_{\text{app,max}} = 2$ V. Interestingly, in all cases, the
 390 optimum association constant was $\beta_{\text{KL}} = 100$ M $^{-1}$. Even though larger concentrations
 391 of ionophores induce more ionic release, we chose $[\text{L}]_{\text{tot}} = 200$ mM corresponding to half
 392 of the maximum steric occupancy of a very common K^+ -ionophore [65]. Therefore, the
 393 optimum from Fig. S7.b was used, i.e., $[\text{PSS}^-] = 637$ mM. Further analysis regarding
 394 the maximum voltage applied at the CP electrode, $V_{\text{app,max}}$, revealed that the optimum
 395 amount of $[\text{PSS}^-]$ depends on this parameter with direct proportionality (Fig. S7.d)
 396 but changes on the above-defined figure of merit are modest (Fig. S7.e).

397 Figure 7 reports the simulation results for ion actuation in the ionoCP case study
 398 with the optimized parameters described above. Here, ionophores L are embedded
 399 in the CP and provide selectivity to K^+ ions by forming K^+ -L complexes (hereafter,
 400 simply KL). The formation process is shown in Fig. 7.a, where a CP pre-charged with
 401 Na^+ is immersed into the extracellular fluid and held at the dedoped state $V_{\text{app}} = -1$
 402 V while ionophores bind the free K^+ ions entering from the ECF. At equilibrium,
 403 the ratio between potassium (both free and complexed) and sodium ions in the CP
 404 results larger than in the ECF (and thus larger than in the nsCP case seen in Fig. 6).
 405 Specifically, we observe $[\text{K}^+]_{\text{CP}} = 14.9$ mM, $[\text{KL}] = 119.8$ mM, $[\text{Na}^+]_{\text{CP}} = 537.1$ mM, and
 406 so $([\text{K}^+]_{\text{CP}} + [\text{KL}])/[\text{Na}^+]_{\text{CP}} = 25.1\%$ (instead of 2.8% as in the nsCP case).

407 Figure 7.b and c show two examples of ionic actuation with the ionoCP, for $v = 10$
 408 V/s and $v = 40$ V/s, respectively ($V_{\text{app,max}} = 1$ V). Because of the selectivity induced by
 409 the ionophores and their relatively low association constant, a much higher perturbation
 410 of $[\text{K}^+]$ is obtained with respect to the non-selective case of Fig. 6. However, the main
 411 hallmark of the ionophores' presence is the prolonged release of K^+ due to the unbinding
 412 of the KL complexes that continues for several hundreds of ms after the end of the V_{app}
 413 ramp (compare Fig. 7.b and Fig. 6.b). This is also shown in Fig. S8, where the local
 414 $[\text{K}^+]$ at the bottom of the neuron is plotted for different $V_{\text{app,max}}$ and for different time
 415 snapshots after the end of the release, in both the ionoCP and nsCP cases. Fig. 7.c
 416 shows that an AP is obtained by increasing v to 40 V/s. Interestingly, a closer analysis
 417 revealed that such AP is a mixed ionic/electric AP since it is not elicited if the reversal
 418 potentials are kept fixed to their baseline values (see Fig. S9). In other words, the
 419 K^+ -induced depolarization lowers the threshold for electrical stimulation necessary to
 420 induce firing.

421 An important feature of the ionoCP device, is the possibility of operating with
 422 a single reservoir (i.e., the ECF) as a recyclable source of ions. Figure 8 shows a
 423 preliminary investigation of this possibility. Namely, we considered actuation transients
 424 with voltage pulses featuring both rise and fall ramps, possibly with different slopes.
 425 The falling ramp allows the CP to return to its dedoped state and thus recharged with

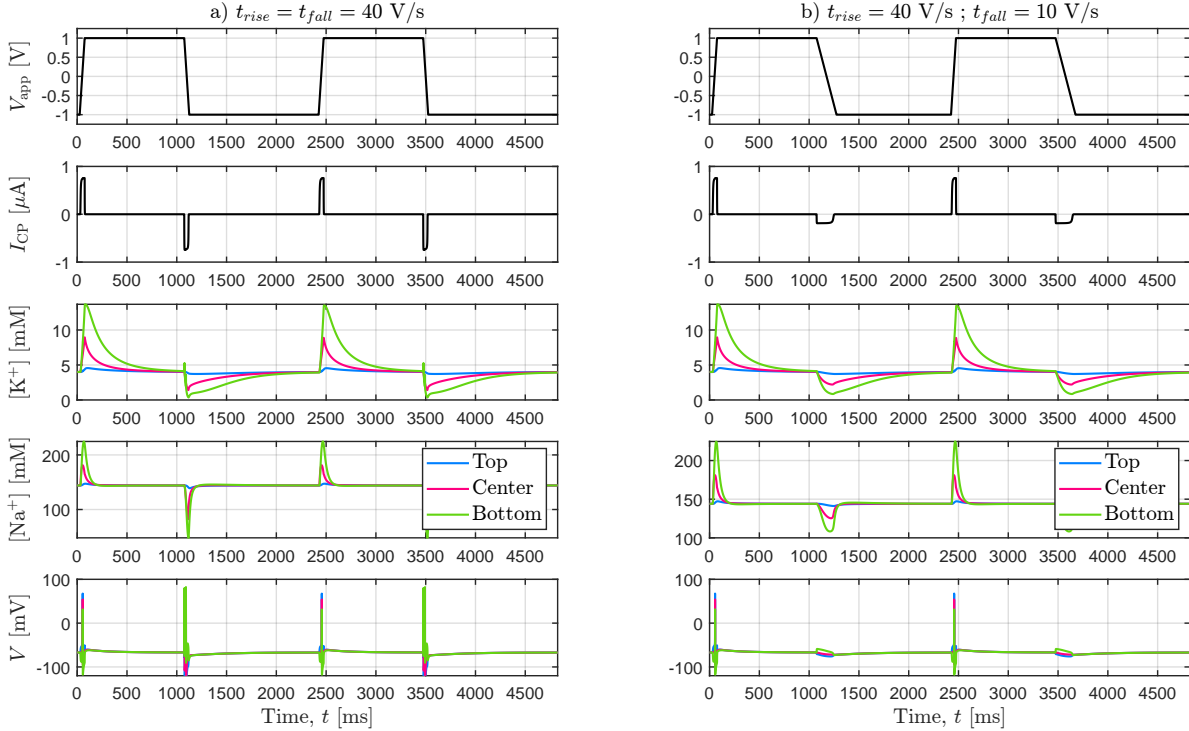


Figure 8. Test of the reversibility of the operation of the ionophores-induced selective CP (ionoCP). Potential pulses with different rise and fall times are applied at the CP during the actuation cycle. From top to bottom, rows indicate: 1) the voltage applied to the CP V_{app} , 2) the current emitted by the CP, $I_{CP} = F \frac{d}{dt} (\int_{CP} p d\Omega)$, the extracellular concentration of 3) $[K^+]$, and 4) $[Na^+]$, and, 5), the membrane potential V . In a), fast slopes of 40 V/s are used for both rising and falling edges, causing electrically-induced APs at each front followed by a gradual return to the electrochemical equilibrium. In b), a slower slope of 10 V/s is used on the falling edge (i.e., return to baseline) that does not induce APs. Besides, two consecutive pulses are displayed for both cases, showing no perceptible difference in the second pulse compared to the first one in terms of potential waveform and ionic profiles. An interesting observation is that the ionic emission and recharge dynamics are very different, as they reflect two different mechanisms: the first one is the ionic release limited by K^+ diffusion to the bulk of the extracellular fluid, while the second one is the depletion of ions in the proximity of the CP/electrolyte interface, ultimately limited by the diffusion of ions from the bulk to the solution.

426 ions diffusing from the ECF. We extended the simulation time to include many pulses,
 427 thereby showing that a full recovery of the baseline equilibrium between CP and ECF is
 428 achieved in less than 1 s after the falling ramp. Figure 8 also indicates that the return to
 429 baseline of the potential applied to the CP (or, in other words, the CP recharge of ionic
 430 carriers) can be seen as an actuation mechanism as well, since the descending voltage
 431 ramp can induce both potential and ion concentration perturbations in the electrolyte.
 432 The rate of the recovering step will thus determine the extent of the actuation both in
 433 terms of modulation of the ionic concentrations and in terms of the transient electric
 434 field in the extracellular domain surrounding the neuron.

435 The analysis above suggests that, despite not being sufficient to handle a fully ionic
 436 neuromodulation, the functionalized ionoCP is still able to enhance the excitability of
 437 the neuron and to operate in a reversible fashion. The reader should note that ionophores

438 are here modeled as mobile species in our framework. However, this is not a critical
 439 choice since results are very mildly affected by considering such species to be covalently
 440 bound to the polymer backbone or with very low diffusion coefficients (see Fig. S10).

441 3.4. Ionophores-induced selective CP (ionoCP): effect on AMPA synapses

442 To further test the neuromodulation capabilities of the ionoCP film, we evaluate the
 443 response of the neuron undergoing ionic actuation in the presence of an excitatory
 444 synaptic event. First, we determined the synaptic conductances $\bar{g}_{K,syn}$, $\bar{g}_{Na,syn}$ (see
 445 Fig. 2, right) as the minimum values required to elicit APs (see Fig. S11). Thus, we
 446 investigated the efficacy of synaptic transmission for different scaling of the synaptic
 447 conductances and for increasing extents of ionic release (see Fig. 9). We point out
 448 that, since the neural membrane is described by a reduced HH model [43], the $\bar{g}_{X_i,syn}$
 449 are regarded as phenomenological terms lumping the postsynaptic conductances of all
 450 the AMPA synaptic receptors, rather than the dynamics of a single synapse. In this
 451 perspective, variations of $\bar{g}_{X_i,syn}$ qualitatively represent changes in the presynaptic drive
 452 to the neuron. Figure 9.a shows a synaptic event occurring 30 ms after an ionic actuation
 453 transient that fails to induce an AP ($0.4 g_{X_i,syn}$, $V_{app,max} = 0$ V). Successful synaptic
 454 transmission can be achieved through larger presynaptic drive ($0.7 g_{X_i,syn}$ in Fig. 9.b)
 455 or more ionic release ($V_{app,max} = 1$ V) in Fig. 9.c, since the postsynaptic current gets
 456 enhanced. Figures 9.A-F illustrate a more extensive study, where elicited APs are
 457 mapped in the two-dimensional space of synaptic conductances scaling – extent of ionic
 458 release, for different delays between ionic stimulation and the synaptic event. These
 459 results clearly suggest that excitatory synaptic transmission is facilitated in the presence
 460 of the ionic actuators releasing K^+ . Moreover, thanks to the slow release granted by
 461 ionophores, such facilitation lasts up to hundreds of milliseconds with progressively
 462 milder intensity.

463 4. Discussion

464 4.1. Modeling of neuromodulation through ionic actuators

465 In this work, we introduced a finite-element model to describe the interaction between
 466 a CP-coated microelectrode and a neuron soma. To the extent of our knowledge, this is
 467 the first computational framework that solves the coupled equations for the dynamics of
 468 an ionic actuator, the cellular fluids, and the neural membrane. We used our simulation
 469 framework to investigate the controlled delivery of potassium in the extracellular fluid
 470 as a neuromodulation mean. We considered three case studies for the CP, with different
 471 levels of selectivity to K^+ : ideally-selective (isCP), non-selective (nsCP), and ionophores-
 472 induced selective (ionoCP).

473 The isCP case, despite being unrealistic, allowed us to showcase the technological
 474 potential of ionic neuromodulation assuming a CP film able to selectively store and
 475 release in the ECF only potassium. A local increase of $[K^+]$ allows steering a target

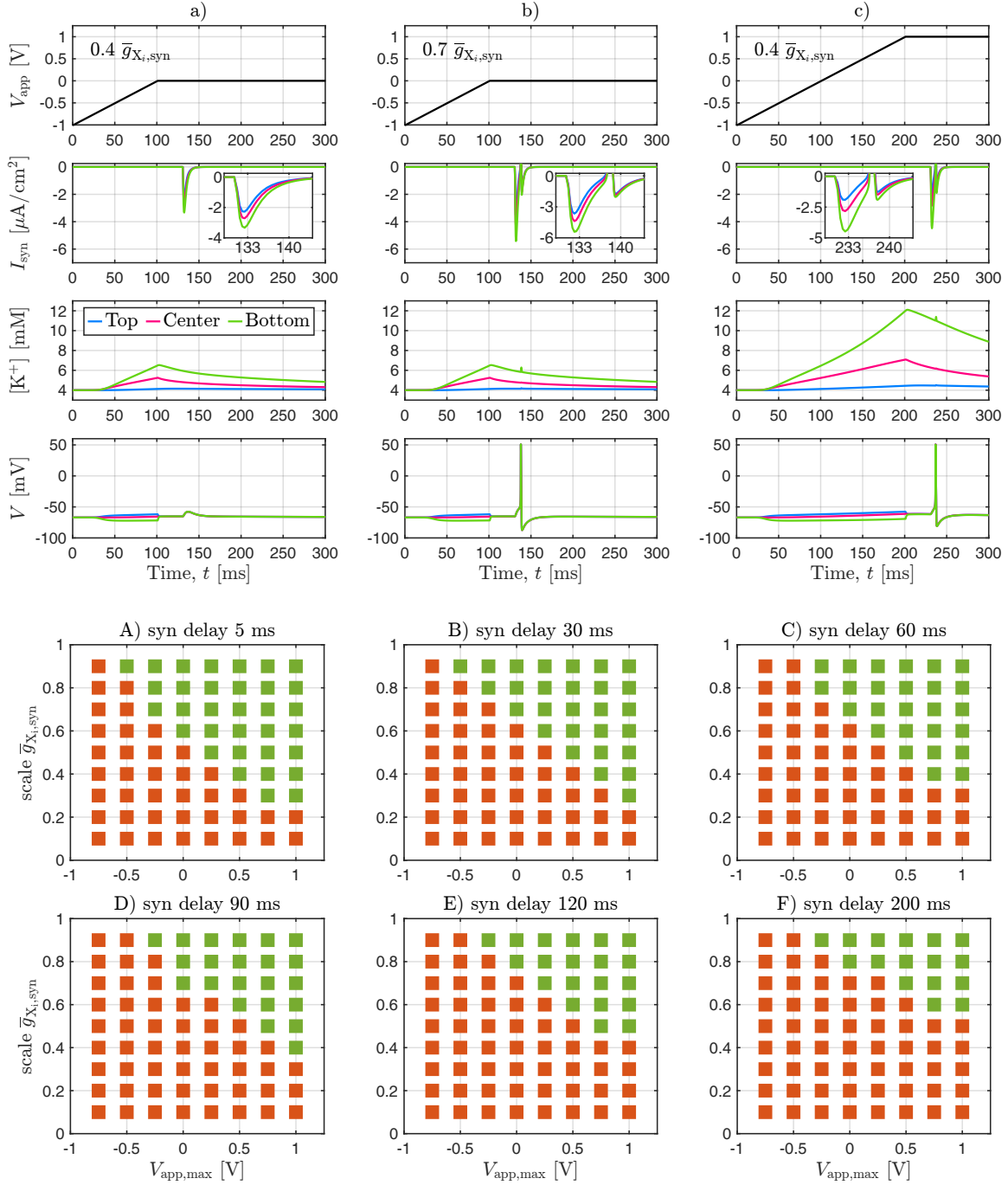


Figure 9. Ionophores-induced selective CP (ionoCP) and synaptic transmission. Top) Examples of synaptic events taking place 30 ms after the end of the ionic release. The one in a) fails to induce an AP ($0.4 \bar{g}_{X_i, syn}$, $V_{app, max} = 0$ V). Successful synaptic transmission can be achieved by increasing the postsynaptic current with, e.g., b) a larger presynaptic drive ($0.7 \bar{g}_{X_i, syn}$) or c) higher applied potential ($V_{app, max} = 1$ V). The rows show, in order: 1) the potential applied to the CP, 2) the synaptic current $I_{syn} = I_{K, syn} + I_{Na, syn}$ 3) the extracellular concentrations for K^+ , and 4) the membrane potential. Bottom) Systematic evaluation of the synaptic transmission's efficacy in the space of $V_{app, max}$ and the scaling of $\bar{g}_{X_i, syn}$. Each subplot corresponds to a different delay between the synaptic event and the end of ionic release. In order, from A to F: 5, 30, 60, 90, 120, and 200 ms. Green squares: AP elicited. Red squares: no AP elicited.

476 neuron to regimes of firing or depolarization block by affecting its intrinsic excitability.
 477 These are well-established facts in literature [66], which can be leveraged to elicit or
 478 inhibit neural activity, respectively. We note that, regarding inhibition, depolarization
 479 block is a mechanism putatively exploited by neurons to limit the overall network activity
 480 also *in-vivo* [67]. A FEM modeling framework enables to link such neuromodulation
 481 targets to the physical and geometrical parameters of the CP and its surroundings, as
 482 well as the stimulation protocols. Examples of such capabilities have been showcased
 483 by changing the potential waveform applied to the CP, the maximum releasable dose
 484 of potassium, the lateral encumbrance due to other cells, and the size of the CP-
 485 neuron cleft. Notwithstanding, similar analyses can be performed for all the other
 486 model parameters, e.g., the CP size, the material of the metal contact, or other intrinsic
 487 parameters of the CP, such as the volumetric capacitance, in support of thoughtful
 488 engineering choices.

489 At the opposite side of the selectivity spectrum, the nsCP case illustrates how a
 490 bare PEDOT:PSS-coated electrode is not effective as ionic neuromodulator. Indeed, it
 491 is not able to hold a pre-charged potassium dose, e.g., coming from a preconditioning
 492 stage in a different electrolyte. Further, it mainly conveys electric stimuli to target
 493 neurons. This is an important sanity check for our simulation deck, since such coatings
 494 are routinely used in electric neurostimulation devices to enhance properties such as
 495 contact impedance, charge storage capacitance, and biocompatibility [68], [69], and our
 496 model confirms that such electrodes can elicit APs through electrical stimulation but
 497 not via ionic perturbation.

498 The ionoCP case is investigated as a possible ionic neuromodulation device endowed
 499 with ionophores that confer selectivity. Indeed, the possibility to embed ionophores in
 500 the polymeric backbones has already been proven in the literature [21]–[23], even though
 501 they were employed for ion-sensing devices rather than for ion delivery. A second
 502 important challenge addressed by our solution is the operation in a single reservoir,
 503 i.e., the ECF, which holds the promise to act as a recyclable source of ions to perform
 504 unlimited stimulation, reconciling miniaturization without handling multiple reservoirs
 505 as in other iontronic solutions [13], [70]. Our findings suggest that ionophores with an
 506 equilibrium constant around $\beta_{\text{KL}} = 100 \text{ M}^{-1}$ give the best trade-off between selectivity
 507 and release performance. This value is smaller than those used in sensor applications
 508 (e.g., $\beta_{\text{KL}} = 1026.2 \pm 118.3 \text{ M}^{-1}$ in [21]) as too strong complexes are difficult to dissociate
 509 during the actuation phase. Notwithstanding, our framework can be utilized to test
 510 realistic ionophore species [71], [72], by instantiating the respective parameters. With
 511 the optimized ionoCP, we have shown *in-silico* that, despite its performances being
 512 highly inferior with respect to the isCP, it is still possible to induce a significant local
 513 perturbation of $[\text{K}^+]$ up to tens of mM above the extracellular bulk concentration,
 514 sufficient to enhance the sensitivity of the neuron to other stimulation means (e.g.,
 515 electrical stimulation), as well as to facilitate excitatory synaptic transmission. A similar
 516 neuromodulation capability was recently proven *ex-vivo* in retina tissue by microfluid
 517 delivery of Ames’ medium containing 22 mM K^+ on perforated microelectrode arrays

518 [73]. This suggests that induced synaptic facilitation provided by ionic neuromodulation
519 may also represent a mean to trigger synaptic plasticity in networks of neurons.

520 The above analysis led us to conclude that it is difficult to elicit APs by releasing
521 potassium ions only, unless an ideally selective polymer is available. In case the polymer
522 is not selective or only partially selective, APs are essentially elicited by electrical
523 stimulation if the electrode potential is ramped fast, but this cannot be referred to
524 as *ionic actuation*. Further, ideal selectivity for actuation purposes is very hard to
525 achieve with ionophores. The inclusion of synaptic dynamics showed that effects on
526 neural activity driven by ionic actuation are more pronounced through the synaptic
527 pathway rather than those affecting the intrinsic excitability of the neuron. These
528 analyses, despite being qualitative, prompt the need for a description of neuronal
529 dynamics down to the level of synaptic transmission to correctly predict the effects of
530 ionic actuation. Since synaptic dynamics is intrinsically a network phenomenon, more
531 effort must be made to increase the complexity of the simulation deck, while ensuring a
532 viable computational cost. We remark that our conclusions, despite being obtained *in-*
533 *silico*, are build upon models that have been extensively validated against experiments.
534 Indeed, the two-phase model for the CP has been shown to effectively fit electrochemical
535 data [28]. Moreover, the HH model [43], coupled with lumped dynamics of ions in the
536 cellular fluid, was able to qualitatively capture the firing patterns of interneurons of the
537 rat CA1 hippocampus in seizure-like and spreading depression-like events [50], [51].

538 4.2. Simulation platform

539 Our approach based on COMSOL Multiphysics enables seamless integration with other
540 stimulation or sensing devices that may be relevant in neuromodulation applications,
541 like multielectrode arrays (MEAs) [74]. Moreover, the use of a commercial platform
542 has been motivated by its widespread adoption in the computational communities of
543 neuroengineering [33], [34] and electrochemistry [28]–[32], and by its capabilities in
544 bridging the gaps between these two disciplines: the former being very knowledgeable in
545 terms of modeling neural activity and excitation but relying on an ohmic description of
546 the neural milieu, while the latter focusing on the electrodiffusive description of cellular
547 fluids but without taking into account the effects on neuronal activity. We point out
548 that this is an alternative approach compared to that of the computational neuroscience
549 community dealing with drift-diffusion phenomena in the neural microenvironment [39],
550 [75]–[78], which typically embraces open-source software.

551 4.3. Model limitations and outlook

552 In this work, we resorted to the PNP model to describe ion electrodiffusion in the cellular
553 fluids. Modeling neural activity with such a level of detail is very computationally
554 demanding and therefore difficult to scale to large spatial domains and more complex
555 geometries. The main reason resides in the building up of electrical double layers at
556 charged interfaces that require very fine spatial meshes with subnanometer resolution.

557 Therefore, studies in the literature employing this formalism have been hitherto limited
558 to simple neural morphologies such as axons [39]. Alternatively, other studies have
559 focused on neural microdomains [41], [42] with small spatial extension, like nodes of
560 Ranvier [40], spines [79], ion channels [80], and synapses [81]. As an example of the
561 aforementioned computational burden, we observed an average simulation time of about
562 26 minutes for the studies reported in Fig. 9.B (89 transients lasting 300 ms), while
563 about 33 minutes for those in Fig. 9.D (89 transients lasting 400 ms). Simulations were
564 run in parallel on two servers: the first with an Intel[®] Xeon[®] X5690 CPU and 189 GB
565 of RAM while the second with an Intel[®] Xeon[®] Gold 6136 CPU and 500 GB of RAM.
566 Further details are reported in Supplementary Note 1. It is thus clear that a reduction in
567 the computational burden is pivotal to pave the way to more realistic descriptions of the
568 *in-vivo* neural milieu, e.g., accounting for detailed neuron morphologies [82] and network
569 interactions [83]. This, in turn, holds the promise to make the presented framework more
570 informative for the design and optimization of ionic actuators, and allows it to handle
571 more complex and realistic cases needed for proper validation against experimental data.

572 Aiming in this direction, the Kirchhoff-Nernst-Planck (KNP) framework has been
573 developed [58], [75]–[78], [84]. It sensibly reduces the computational burden by enforcing
574 electroneutrality in the resolved space domain and splitting displacement currents among
575 ionic fluxes at the cell membranes. However, the validity of KNP has been assessed
576 for biological electrogenic sources [85] but not during the operation of ionic actuators.
577 Indeed, to date, computation efforts focusing on the sole ionic actuator rely on the
578 PNP [29]–[32]. Before deploying the KNP in our setting, its domain of validity must be
579 determined taking into account the tiny clefts and non-physiological ionic concentrations
580 that may stem from the neuron-CP interaction. A preliminary analysis is shown in Fig.
581 S12, where we report the charge density in the cleft between the CP and the neuron
582 under the ion release by the ionoCP (Fig. S12.a) or the nsCP (Fig. S12.b). Further,
583 we consider the charge in the cleft during a synaptically-induced AP (Fig. S12.c), as an
584 example of physiological electrogenic source. Except for the starting and ending phases
585 of the applied stimulus ramp, at each time point the charge in (b) is similar to that in
586 (c). On the other hand, the charge results more than ten times greater in (a) than in
587 (c). This deviation from electroneutrality persists for the entire duration of ionic release
588 in (a) (hundreds of ms) instead of a single AP’s duration in (c) (a few ms). These
589 results suggest that the electroneutrality assumption embraced by the KNP might not
590 hold under the operation of ionic actuators like the ionoCP. A thorough comparison of
591 the PNP model used in this work with a KNP-based model is not in the scope of this
592 work and is left for future investigation.

593 It is important to remark that in our approach the dynamics of the cellular fluids and
594 the ionic actuator are solved self-consistently. This modeling scheme is rarely pursued,
595 even in established computational frameworks supporting the design of neural interfaces,
596 e.g. for electrical stimulation [86], [87]. Rather, scientists resort to *hybrid models*: first,
597 the extracellular potential is computed with either analytical approximations [37] or
598 finite-element methods (FEM) [38]; second, the response of nerve cells is assessed by

599 feeding the results of the previous step as input. Similar schemes have been developed
600 also for electrodiffusive models of the neuron-ECF interaction [75]. Assessing the
601 validity of these schemes in the ionic neuromodulation setting may provide further
602 means to reduce the computational cost, thanks to the decoupling of simulations in two
603 problems easier than the original one. To this aim, our model may be instrumental in
604 validating such simplifications. Another advantage of hybrid approaches is to deploy
605 the full potential of simulators of realistic multicompartment models of nerve cells,
606 like NEURON [88], accounting for complex morphological and dynamical features.
607 Unfortunately, our self-consistent framework in COMSOL does not allow us to delegate
608 the solution of the neural membrane dynamics to third-party software. This limits the
609 integration and reusability of models of neural cells previously published in literature
610 [89].

611 The electrodiffusive formalism employed in this work, as well as the KNP mentioned
612 above, are intrinsically more accurate than the ohmic formalism, where the cellular
613 fluids are considered volume conductors and diffusion mechanisms are neglected. Given
614 its simplicity and low computational cost, the ohmic formalism is widely used to
615 model the interface between neurons and implanted electrodes, both for stimulation
616 [34] and recording [90] studies. However, the lack of a proper description of the ionic
617 transport limits the validity to cases where the electric field is the main vehicle of
618 action potential recording/generation. In Supplementary Note 2 (Sec. “Limit case:
619 ohmic approximation for cellular fluids”) we introduce the main equations of the ohmic
620 formalism and show that, in fact, its predictions agree with our model only in limit
621 cases where the cleft between the CP and the neuron is sufficiently large such that
622 the modulations of the ionic concentrations are relatively small. In this comparison,
623 we employed the nsCP since, among our case studies, is the one that best reproduces
624 electrodes routinely used in scenarios of electrical neural stimulation/recording (see Sec.
625 4.1).

626 We built our modeling framework with the aim of having the essential features to
627 serve as a benchmark for testing the neuromodulation capabilities of the ionic actuator.
628 The selected features resulted from a compromise between the computational burden of
629 simulations and the spatio-temporal scales of interest, namely those of a single neuron
630 soma discharging up to a few APs, thereby leading to several simplifications. On the
631 neural milieu’s side, we modeled the dynamics of K^+ , Na^+ , and Cl^- ions, along with
632 the ion channels responsible for the sole generation of action potentials. However, many
633 other ions [1], like Ca^{2+} or Mg^{2+} , and ionic channels [36] affects the neural functioning.
634 Furthermore, we neglected homeostatic mechanisms occurring at neural membranes or
635 glial cells that are pivotal for the regulation of the ionic composition in the neural
636 microenvironment [2] and are expected to counteract the operation of ionic actuators.
637 Nevertheless, the effects of such mechanisms manifest at temporal scales longer than
638 the ones of interest in this work. A possible way to capitalize on the aforementioned
639 efforts to reduce the computational burden would be the inclusion of such mechanisms
640 and gain insight into the effects of ionic actuation at longer temporal scales. Similar

641 considerations apply also to the CP's side, where many non-idealities and parasitic
642 phenomena were neglected. For instance: faradaic conduction in the CP [91], the
643 formation of competing bindings of ionophores with, e.g., Na^+ ions [21], series impedance
644 of the electrodes [59], as well as red-ox reaction between the CP and the cellular fluids
645 [55]. Other model simplifications are the usage of uniform and time-invariant parameter
646 values inside domains, in contrast with time variability and reduced ionic diffusivity due
647 to tortuosity effects in the ECF [92], as well as variability in the density of ion channels in
648 different portions of the membrane [93]. Notwithstanding, our multiphysics framework
649 is amenable for the integration of these features to explore their effects on the device
650 performance.

651 5. Conclusion

652 This work combines the multiphysical description of the most essential set of
653 electrochemical and biological processes regarding neurons under ionic and electrical
654 stimulation in a single comprehensive simulation deck. By including accurate models of
655 ion-transport and transmembrane fluxes we demonstrated *in-silico* that the proposed
656 modeling approach can be a powerful tool to predict neuron excitability and to
657 benchmark the performance of novel neuromodulation devices. As an example of
658 application, we simulated the action of an ionic actuator based on organic mixed
659 ionic-electronic conductors (OMIECs) embedding ionophores and demonstrated its
660 capability to provide single-neuron synaptic facilitation. These efforts are oriented
661 toward versatile integration with iontronic devices aiming at closing the loop of already
662 existing methodologies for neural recording and computation *in-liquido* [94].

663 Acknowledgments

664 This work was supported by the European Union's Horizon 2020 Research and
665 Innovation Programme (IN-FET Project) via the Consorzio Nazionale Interuniversitario
666 per la Nanoelettronica (IU. NET) Consortium under Grant Agreement 862882.

667 References

- 668 [1] R. Rasmussen, J. O'Donnell, F. Ding, and M. Nedergaard, "Interstitial ions: A key
669 regulator of state-dependent neural activity?" *Progress in Neurobiology*, vol. 193,
670 2020. DOI: 10.1016/j.pneurobio.2020.101802.
- 671 [2] G. G. Somjen, *Ions in the Brain: Normal Function, Seizures, and Stroke*. Oxford
672 University Press, 2004, ISBN: 9780195151718.
- 673 [3] B. Frankenhaeuser and A. L. Hodgkin, "The after-effects of impulses in the giant
674 nerve fibres of *Loligo*," *The Journal of physiology*, vol. 131, no. 2, 1956. DOI:
675 10.1113/jphysiol.1956.sp005467.

- 676 [4] M. Balestrino, P. G. Aitken, and G. G. Somjen, “The effects of moderate changes
677 of extracellular K^+ and Ca^{2+} on synaptic and neural function in the CA1 region of
678 the hippocampal slice,” *Brain Research*, vol. 377, no. 2, 1986. DOI: 10.1016/0006-
679 8993(86)90863-2.
- 680 [5] P. Y. Shih, L. P. Savtchenko, N. Kamasawa, *et al.*, “Retrograde Synaptic Signaling
681 Mediated by K^+ Efflux through Postsynaptic NMDA Receptors,” *Cell Reports*,
682 vol. 5, no. 4, 2013. DOI: 10.1016/j.celrep.2013.10.026.
- 683 [6] L. M. Grover and T. J. Teyler, “Effects of extracellular potassium concentration
684 and postsynaptic membrane potential on calcium-induced potentiation in area
685 CA1 of rat hippocampus,” *Brain Research*, vol. 506, no. 1, 1990. DOI: 10.1016/
686 0006-8993(90)91198-P.
- 687 [7] D. M. Durand, E. H. Park, and A. L. Jensen, “Potassium diffusive coupling in
688 neural networks,” *Philosophical Transactions of the Royal Society B: Biological
689 Sciences*, vol. 365, no. 1551, 2010. DOI: 10.1098/rstb.2010.0050.
- 690 [8] J. V. Raimondo, R. J. Burman, A. A. Katz, and C. J. Akerman, “Ion dynamics
691 during seizures,” *Frontiers in Cellular Neuroscience*, vol. 9, no. OCT, 2015. DOI:
692 10.3389/fncel.2015.00419.
- 693 [9] S. F. Traynelis and R. Dingledine, “Potassium-induced spontaneous electrographic
694 seizures in the rat hippocampal slice,” *Journal of Neurophysiology*, vol. 59, no. 1,
695 1988. DOI: 10.1152/jn.1988.59.1.259.
- 696 [10] D. Pietrobon and M. A. Moskowitz, “Chaos and commotion in the wake of
697 cortical spreading depression and spreading depolarizations,” *Nature Reviews
698 Neuroscience*, vol. 15, no. 6, 2014. DOI: 10.1038/nrn3770.
- 699 [11] A. J. Hansen and T. Zeuthen, “Extracellular ion concentrations during spreading
700 depression and ischemia in the rat brain cortex,” *Acta Physiologica Scandinavica*,
701 vol. 113, no. 4, 1981. DOI: 10.1111/j.1748-1716.1981.tb06920.x.
- 702 [12] G. Ullah and S. J. Schiff, “Tracking and control of neuronal Hodgkin-Huxley
703 dynamics,” *Physical Review E - Statistical, Nonlinear, and Soft Matter Physics*,
704 vol. 79, no. 4, 2009. DOI: 10.1103/PhysRevE.79.040901.
- 705 [13] J. Isaksson, P. Kjäll, D. Nilsson, N. Robinson, M. Berggren, and A. Richter-
706 Dahlfors, “Electronic control of Ca^{2+} signalling in neuronal cells using an organic
707 electronic ion pump,” *Nature Materials*, vol. 6, no. 9, 2007. DOI: 10.1038/
708 nmat1963.
- 709 [14] I. Uguz, C. M. Proctor, V. F. Curto, *et al.*, “A Microfluidic Ion Pump for In Vivo
710 Drug Delivery,” *Advanced Materials*, vol. 29, no. 27, 2017. DOI: 10.1002/adma.
711 201701217.
- 712 [15] C. M. Proctor, I. Uguz, A. Slezia, *et al.*, “An Electrocardiography Device with
713 an Integrated Microfluidic Ion Pump for Simultaneous Neural Recording and
714 Electrophoretic Drug Delivery In Vivo,” *Advanced Biosystems*, vol. 3, no. 2, 2019.
715 DOI: 10.1002/adbi.201800270.

- 716 [16] M. Berggren, E. D. Głowacki, D. T. Simon, E. Stavrinidou, and K. Tybrandt, “In
717 Vivo Organic Bioelectronics for Neuromodulation,” *Chemical Reviews*, vol. 122,
718 no. 4, pp. 4826–4846, 2022. DOI: 10.1021/acs.chemrev.1c00390.
- 719 [17] B. D. Paulsen, K. Tybrandt, E. Stavrinidou, and J. Rivnay, “Organic mixed
720 ionic–electronic conductors,” *Nature Materials*, vol. 19, no. 1, 2020. DOI: 10.1038/
721 s41563-019-0435-z.
- 722 [18] Z. J. Du, G. Q. Bi, and X. T. Cui, “Electrically Controlled Neurochemical Release
723 from Dual-Layer Conducting Polymer Films for Precise Modulation of Neural
724 Network Activity in Rat Barrel Cortex,” *Advanced Functional Materials*, vol. 28,
725 no. 12, 2018. DOI: 10.1002/adfm.201703988.
- 726 [19] K. M. Woeppel, X. S. Zheng, Z. M. Schulte, N. L. Rosi, and X. T. Cui,
727 “Nanoparticle Doped PEDOT for Enhanced Electrode Coatings and Drug
728 Delivery,” *Advanced Healthcare Materials*, vol. 8, no. 21, 2019. DOI: 10.1002/
729 adhm.201900622.
- 730 [20] C. Tan, N. Kushwah, and X. T. Cui, “Electrically controlled neurochemical
731 delivery from microelectrodes for focal and transient modulation of cellular
732 behavior,” *Biosensors*, vol. 11, no. 9, 2021. DOI: 10.3390/bios11090348.
- 733 [21] A. Villarroel Marquez, G. Salinas, M. Abarkan, *et al.*, “Design of Potassium-
734 Selective Mixed Ion/Electron Conducting Polymers,” *Macromolecular Rapid
735 Communications*, vol. 41, no. 12, 2020. DOI: 10.1002/marc.202000134.
- 736 [22] S. Wustoni, C. Combe, D. Ohayon, M. H. Akhtar, I. McCulloch, and S. Inal,
737 “Membrane-Free Detection of Metal Cations with an Organic Electrochemical
738 Transistor,” *Advanced Functional Materials*, vol. 29, no. 44, 2019. DOI: 10.1002/
739 adfm.201904403.
- 740 [23] M. Jeszke, K. Trzciński, J. Karczewski, and E. Luboch, “Investigation of poly(3,4-
741 ethylenedioxythiophene) deposition method influence on properties of ion-selective
742 electrodes based on bis(benzo-15-crown-5) derivatives,” *Electrochimica Acta*,
743 vol. 246, 2017. DOI: 10.1016/j.electacta.2017.05.197.
- 744 [24] M. Sessolo, J. Rivnay, E. Bandiello, G. G. Malliaras, and H. J. Bolink, “Ion-
745 selective organic electrochemical transistors,” *Advanced Materials*, vol. 26, no. 28,
746 pp. 4803–4807, 2014. DOI: 10.1002/adma.201400731.
- 747 [25] R. M. Owens, S. Daniel, A. M. Pappa, *et al.*, “Optical and electronic ion channel
748 monitoring from native human membranes,” *ACS Nano*, vol. 14, no. 10, 2020. DOI:
749 10.1021/acsnano.0c01330.
- 750 [26] T. Arbring Sjöström, M. Berggren, E. O. Gabrielsson, *et al.*, “A Decade of
751 Iontronic Delivery Devices,” *Advanced Materials Technologies*, vol. 3, no. 5, 2018.
752 DOI: 10.1002/admt.201700360.
- 753 [27] A. J. Bard, L. R. Faulkner, and H. S. White, *Electrochemical methods:
754 fundamentals and applications*, 2nd ed. John Wiley & Sons Inc., 2001, ISBN:
755 9780471043720.

- 756 [28] K. Tybrandt, I. V. Zozoulenko, and M. Berggren, “Chemical potential–electric
757 double layer coupling in conjugated polymer–polyelectrolyte blends,” *Science*
758 *advances*, vol. 3, no. 12, eaao3659, 2017. DOI: 10.1126/sciadv.aao3659.
- 759 [29] K. Tybrandt, “Exploring the potential of ionic bipolar diodes for chemical neural
760 interfaces,” *Soft Matter*, vol. 13, no. 44, 2017. DOI: 10.1039/c7sm01732d.
- 761 [30] T. A. Sjöström, A. Jonsson, E. O. Gabrielsson, M. Berggren, D. T. Simon, and K.
762 Tybrandt, “Miniaturized Ionic Polarization Diodes for Neurotransmitter Release
763 at Synaptic Speeds,” *Advanced Materials Technologies*, vol. 5, no. 3, 2020. DOI:
764 10.1002/admt.201900750.
- 765 [31] T. Arbring Sjöström, A. I. Ivanov, C. Bernard, *et al.*, “Design and Operation
766 of Hybrid Microfluidic Iontronic Probes for Regulated Drug Delivery,” *Advanced*
767 *Materials Technologies*, vol. 6, no. 2, 2021. DOI: 10.1002/admt.202001006.
- 768 [32] M. T. Flavin, M. A. Paul, A. S. Lim, *et al.*, “Electrochemical modulation enhances
769 the selectivity of peripheral neurostimulation in vivo,” *Proceedings of the National*
770 *Academy of Sciences*, vol. 119, no. 23, Jun. 2022. DOI: 10.1073/PNAS.2117764119.
- 771 [33] S. Romeni, G. Valle, A. Mazzoni, and S. Micera, “Tutorial: a computational
772 framework for the design and optimization of peripheral neural interfaces,” *Nature*
773 *Protocols*, vol. 15, no. 10, 2020. DOI: 10.1038/s41596-020-0377-6.
- 774 [34] A. Fellner, A. Heshmat, P. Werginz, and F. Rattay, “A finite element
775 method framework to model extracellular neural stimulation,” *Journal of Neural*
776 *Engineering*, vol. 19, no. 2, p. 022001, Apr. 2022. DOI: 10.1088/1741-2552/
777 AC6060.
- 778 [35] R. Plonsey and R. C. Barr, *Bioelectricity: A quantitative approach*. Springer, 2007,
779 ISBN: 9780387488646. DOI: 10.1007/978-0-387-48865-3.
- 780 [36] D. Sterratt, B. Graham, A. Gillies, and D. Willshaw, *Principles of computational*
781 *modelling in neuroscience*. Cambridge University Press, 2011. DOI: 10.1017/
782 CB09780511975899.
- 783 [37] H. Lindén, E. Hagen, S. Leski, E. S. Norheim, K. H. Pettersen, and G. T. Einevoll,
784 “LFPy: A tool for biophysical simulation of extracellular potentials generated by
785 detailed model neurons,” *Frontiers in Neuroinformatics*, vol. 7, no. JAN, 2014.
786 DOI: 10.3389/fninf.2013.00041.
- 787 [38] C. H. Lubba, Y. Le Guen, S. Jarvis, *et al.*, “PyPNS: Multiscale Simulation of
788 a Peripheral Nerve in Python,” *Neuroinformatics*, vol. 17, no. 1, 2019. DOI: 10.
789 1007/s12021-018-9383-z.
- 790 [39] J. Pods, J. Schönke, and P. Bastian, “Electrodiffusion models of neurons
791 and extracellular space using the poisson-nernst-planck equations - Numerical
792 simulation of the intra- and extracellular potential for an axon model,” *Biophysical*
793 *Journal*, vol. 105, no. 1, 2013. DOI: 10.1016/j.bpj.2013.05.041.

- 794 [40] C. L. Loppreore, T. M. Bartol, J. S. Coggan, *et al.*, “Computational modeling of
795 three-dimensional electrodiffusion in biological systems: Application to the node
796 of Ranvier,” *Biophysical Journal*, vol. 95, no. 6, 2008. DOI: 10.1529/biophysj.
797 108.132167.
- 798 [41] D. Holcman and R. Yuste, “The new nanophysiology: Regulation of ionic flow in
799 neuronal subcompartments,” *Nature Reviews Neuroscience*, vol. 16, no. 11, 2015.
800 DOI: 10.1038/nrn4022.
- 801 [42] L. P. Savtchenko, M. M. Poo, and D. A. Rusakov, “Electrodiffusion phenomena
802 in neuroscience: A neglected companion,” *Nature Reviews Neuroscience*, vol. 18,
803 no. 10, 2017. DOI: 10.1038/nrn.2017.101.
- 804 [43] J. R. Cressman, G. Ullah, J. Ziburkus, S. J. Schiff, and E. Barreto, “The
805 influence of sodium and potassium dynamics on excitability, seizures, and the
806 stability of persistent states: I. single neuron dynamics,” *Journal of computational
807 neuroscience*, vol. 26, no. 2, pp. 159–170, 2009. DOI: 10.1007/s10827-008-0132-
808 4.
- 809 [44] E. Barreto and J. R. Cressman, “Ion concentration dynamics as a mechanism
810 for neuronal bursting,” *Journal of Biological Physics*, vol. 37, no. 3, 2011. DOI:
811 10.1007/s10867-010-9212-6.
- 812 [45] Y. Wei, G. Ullah, and S. J. Schiff, “Unification of neuronal spikes, seizures, and
813 spreading depression,” *Journal of Neuroscience*, vol. 34, no. 35, 2014. DOI: 10.
814 1523/JNEUROSCI.0516-14.2014.
- 815 [46] M. Kalia, H. G. Meijer, S. A. van Gils, M. J. van Putten, and C. R. Rose,
816 “Ion dynamics at the energy-deprived tripartite synapse,” *PLoS Computational
817 Biology*, vol. 17, no. 6, 2021. DOI: 10.1371/journal.pcbi.1009019.
- 818 [47] S. A. Contreras, J. H. Schleimer, A. T. Gullledge, and S. Schreiber, “Activity-
819 mediated accumulation of potassium induces a switch in firing pattern and
820 neuronal excitability type,” *PLoS Computational Biology*, vol. 17, no. 5, 2021.
821 DOI: 10.1371/journal.pcbi.1008510.
- 822 [48] H. Kager, W. J. Wadman, and G. G. Somjen, “Simulated seizures and
823 spreading depression in a neuron model incorporating interstitial space and ion
824 concentrations,” *Journal of Neurophysiology*, vol. 84, no. 1, 2000. DOI: 10.1152/
825 jn.2000.84.1.495.
- 826 [49] *Comsol multiphysics user manual*, COMSOL Inc., Sweden, 2022.
- 827 [50] G. Ullah and S. J. Schiff, “Assimilating seizure dynamics,” *PLoS Computational
828 Biology*, vol. 6, no. 5, 2010. DOI: 10.1371/journal.pcbi.1000776.
- 829 [51] Y. Wei, G. Ullah, J. Ingram, and S. J. Schiff, “Oxygen and seizure dynamics: II.
830 Computational modeling,” *Journal of Neurophysiology*, vol. 112, no. 2, 2014. DOI:
831 10.1152/jn.00541.2013.

- 832 [52] A. L. Hodgkin and A. F. Huxley, “A quantitative description of membrane
833 current and its application to conduction and excitation in nerve,” *The Journal*
834 *of Physiology*, vol. 117, no. 4, pp. 500–544, Aug. 1952. DOI: 10.1113/jphysiol.
835 1952.sp004764.
- 836 [53] J. Rivnay, P. Leleux, M. Ferro, *et al.*, “High-performance transistors for
837 bioelectronics through tuning of channel thickness,” *Science Advances*, vol. 1,
838 no. 4, pp. 1–6, 2015. DOI: 10.1126/sciadv.1400251.
- 839 [54] A. V. Volkov, K. Wijeratne, E. Mitraka, *et al.*, “Understanding the Capacitance
840 of PEDOT:PSS,” *Advanced Functional Materials*, vol. 27, no. 28, pp. 1–10, 2017.
841 DOI: 10.1002/adfm.201700329.
- 842 [55] M. O. Bamgbopa, J. Edberg, I. Engquist, M. Berggren, and K. Tybrandt,
843 “Understanding the characteristics of conducting polymer-redox biopolymer
844 supercapacitors,” *Journal of Materials Chemistry A*, vol. 7, no. 41, pp. 23 973–
845 23 980, 2019. DOI: 10.1039/c9ta07030c.
- 846 [56] J. Ehlich, L. Migliaccio, I. Sahalianov, *et al.*, “Direct measurement of
847 oxygen reduction reactions at neurostimulation electrodes,” *Journal of Neural*
848 *Engineering*, vol. 19, no. 3, 2022. DOI: 10.1088/1741-2552/ac77c0.
- 849 [57] L. J. Mele, P. Palestri, M. A. Alam, and L. Selmi, “Selectivity, sensitivity and
850 detection range in ion-selective membrane-based electrochemical potentiometric
851 sensors analyzed with poisson-boltzmann equilibrium model,” *IEEE Sensors*
852 *Journal*, vol. 22, no. 15, pp. 15 010–15 021, 2022. DOI: 10.1109/JSEN.2022.
853 3185168.
- 854 [58] M. J. Sætra, G. T. Einevoll, and G. Halnes, “An electrodiffusive neuron-
855 extracellular-glia model for exploring the genesis of slow potentials in the brain,”
856 *PLoS Computational Biology*, vol. 17, no. 7, 2021. DOI: 10.1371/journal.pcbi.
857 1008143.
- 858 [59] L. J. Mele, C. Verardo, and P. Palestri, “Reproducing capacitive cyclic
859 voltammetric curves by simulation: When are simplified geometries appropriate?”
860 *Electrochemistry Communications*, vol. 142, p. 107 378, 2022. DOI: 10.1016/j.
861 *elecom*.2022.107378.
- 862 [60] M. Bikson, P. J. Hahn, J. E. Fox, and J. G. Jefferys, “Depolarization
863 block of neurons during maintenance of electrographic seizures,” *Journal of*
864 *Neurophysiology*, vol. 90, no. 4, 2003. DOI: 10.1152/jn.00467.2003.
- 865 [61] S. Joucla and B. Yvert, “Modeling extracellular electrical neural stimulation: From
866 basic understanding to MEA-based applications,” *Journal of Physiology Paris*,
867 vol. 106, no. 3-4, 2012. DOI: 10.1016/j.jphysparis.2011.10.003.
- 868 [62] J. K. Krauss, N. Lipsman, T. Aziz, *et al.*, “Technology of deep brain stimulation:
869 current status and future directions,” *Nature Reviews Neurology*, vol. 17, no. 2,
870 2021. DOI: 10.1038/s41582-020-00426-z.

- 871 [63] A. Fitchett, S. Mastitskaya, and K. Aristovich, "Selective Neuromodulation of the
872 Vagus Nerve," *Frontiers in Neuroscience*, vol. 15, 2021. DOI: 10.3389/fnins.
873 2021.685872.
- 874 [64] J. J. Jasielec, T. Sokalski, R. Filipek, and A. Lewenstam, "Neutral-Carrier Ion-
875 Selective Electrodes Assessed by the Nernst-Planck-Poisson Model," *Analytical
876 Chemistry*, vol. 87, no. 17, 2015. DOI: 10.1021/acs.analchem.5b00065.
- 877 [65] K. Neupert-Laves and M. Dobler, "The crystal structure of a k^+ complex of
878 valinomycin," *Helvetica chimica acta*, vol. 58, no. 2, pp. 432–442, 1975. DOI: 10.
879 1002/hlca.19750580212.
- 880 [66] K. Aihara and G. Matsumoto, "Two stable steady states in the Hodgkin-Huxley
881 axons," *Biophysical Journal*, vol. 41, no. 1, 1983. DOI: 10.1016/S0006-3495(83)
882 84408-7.
- 883 [67] D. Bianchi, A. Marasco, A. Limongiello, *et al.*, "On the mechanisms underlying the
884 depolarization block in the spiking dynamics of CA1 pyramidal neurons," *Journal
885 of Computational Neuroscience*, vol. 33, no. 2, 2012. DOI: 10.1007/s10827-012-
886 0383-y.
- 887 [68] M. Bianchi, A. De Salvo, M. Asplund, *et al.*, "Poly(3,4-ethylenedioxythiophene)-
888 Based Neural Interfaces for Recording and Stimulation: Fundamental Aspects and
889 In Vivo Applications," *Advanced Science*, vol. 9, no. 12, 2022. DOI: 10.1002/advs.
890 202104701.
- 891 [69] A. Williamson, M. Ferro, P. Leleux, *et al.*, "Localized Neuron Stimulation with
892 Organic Electrochemical Transistors on Delaminating Depth Probes," *Advanced
893 Materials*, vol. 27, no. 30, pp. 4405–4410, 2015. DOI: 10.1002/adma.201500218.
- 894 [70] A. Jonsson, S. Inal, L. Uguz, *et al.*, "Bioelectronic neural pixel: Chemical
895 stimulation and electrical sensing at the same site," *Proceedings of the National
896 Academy of Sciences of the United States of America*, vol. 113, no. 34, pp. 9440–
897 9445, 2016. DOI: 10.1073/pnas.1604231113.
- 898 [71] P. Bühlmann, E. Pretsch, and E. Bakker, "Carrier-based ion-selective electrodes
899 and bulk optodes. 2. Ionophores for potentiometric and optical sensors," *Chemical
900 Reviews*, vol. 98, no. 4, 1998. DOI: 10.1021/cr970113+.
- 901 [72] Y. Qin, Y. Mi, and E. Bakker, "Determination of complex formation
902 constants of 18 neutral alkali and alkaline earth metal ionophores in poly(vinyl
903 chloride) sensing membranes plasticized with bis(2-ethylhexyl)sebacate and o-
904 nitrophenyloctylether," *Analytica Chimica Acta*, vol. 421, no. 2, 2000. DOI: 10.
905 1016/S0003-2670(00)01038-2.
- 906 [73] A. Esteban-Linares, X. Zhang, H. H. Lee, *et al.*, "Graphene-based microfluidic
907 perforated microelectrode arrays for retinal electrophysiological studies," *Lab on
908 a Chip*, 2023, ISSN: 1473-0189. DOI: 10.1039/D3LC00064H.

- 909 [74] F. Leva, C. Verardo, L. J. Mele, P. Palestri, and L. Selmi, “Multiphysics Finite-
910 Element Modeling of the Neuron/Electrode Electrodiffusive Interaction,” *2022*
911 *IEEE Sensors*, pp. 1–4, Oct. 2022. DOI: 10.1109/SENSOR52175.2022.9967049.
- 912 [75] A. Solbrå, A. W. Bergersen, J. van den Brink, A. Malthe-Sørensen, G. T.
913 Einevoll, and G. Halnes, “A Kirchhoff-Nernst-Planck framework for modeling large
914 scale extracellular electrodiffusion surrounding morphologically detailed neurons,”
915 *PLoS Computational Biology*, vol. 14, no. 10, 2018. DOI: 10.1371/journal.pcbi.
916 1006510.
- 917 [76] A. J. Ellingsrud, A. Solbrå, G. T. Einevoll, G. Halnes, and M. E. Rognes, “Finite
918 Element Simulation of Ionic Electrodiffusion in Cellular Geometries,” *Frontiers in*
919 *Neuroinformatics*, vol. 14, 2020. DOI: 10.3389/fninf.2020.00011.
- 920 [77] A. Tuttle, J. R. Diaz, and Y. Mori, “A computational study on the role
921 of glutamate and NMDA receptors on cortical spreading depression using a
922 multidomain electrodiffusion model,” *PLoS Computational Biology*, vol. 15, no. 12,
923 2019. DOI: 10.1371/journal.pcbi.1007455.
- 924 [78] Y. Mori and C. S. Peskin, “A numerical method for cellular electrophysiology
925 based on the electrodiffusion equations with internal boundary conditions
926 at membranes,” *Communications in Applied Mathematics and Computational*
927 *Science*, vol. 4, no. 1, 2009. DOI: 10.2140/camcos.2009.4.85.
- 928 [79] T. Lagache, K. Jayant, and R. Yuste, “Electrodiffusion models of synaptic
929 potentials in dendritic spines,” *Journal of Computational Neuroscience*, vol. 47,
930 no. 1, 2019. DOI: 10.1007/s10827-019-00725-5.
- 931 [80] R. D. Coalson and M. G. Kurnikova, “Poisson-Nernst-Planck theory approach to
932 the calculation of current through biological ion channels,” *IEEE Transactions on*
933 *Nanobioscience*, vol. 4, no. 1, 2005. DOI: 10.1109/TNB.2004.842495.
- 934 [81] C. L. Gardner, J. R. Jones, S. M. Baer, and S. M. Crook, “Drift-diffusion
935 simulation of the ephaptic effect in the triad synapse of the retina,” *Journal of*
936 *Computational Neuroscience*, vol. 38, no. 1, 2015. DOI: 10.1007/s10827-014-
937 0531-7.
- 938 [82] E. Hay, S. Hill, F. Schürmann, H. Markram, and I. Segev, “Models of neocortical
939 layer 5b pyramidal cells capturing a wide range of dendritic and perisomatic active
940 properties,” *PLoS Computational Biology*, vol. 7, no. 7, 2011. DOI: 10.1371/
941 journal.pcbi.1002107.
- 942 [83] H. Markram, E. Muller, S. Ramaswamy, *et al.*, “Reconstruction and Simulation
943 of Neocortical Microcircuitry,” *Cell*, vol. 163, no. 2, 2015. DOI: 10.1016/j.cell.
944 2015.09.029.
- 945 [84] M. J. Sætra, G. T. Einevoll, and G. Halnes, “An electrodiffusive, ion conserving
946 Pinsky-Rinzel model with homeostatic mechanisms,” *PLoS Computational*
947 *Biology*, vol. 16, no. 4, 2020. DOI: 10.1371/journal.pcbi.1007661.

- 948 [85] J. Pods, “A comparison of computational models for the extracellular potential of
949 neurons,” *Journal of Integrative Neuroscience*, vol. 16, no. 1, 2017. DOI: 10.3233/
950 JIN-170009.
- 951 [86] A. Agudelo-Toro and A. Neef, “Computationally efficient simulation of electrical
952 activity at cell membranes interacting with self-generated and externally imposed
953 electric fields,” *Journal of Neural Engineering*, vol. 10, no. 2, 2013. DOI: 10.1088/
954 1741-2560/10/2/026019.
- 955 [87] S. Joucla, A. Glière, and B. Yvert, “Current approaches to model extracellular
956 electrical neural microstimulation,” *Frontiers in Computational Neuroscience*,
957 vol. 8, no. FEB, 2014. DOI: 10.3389/fncom.2014.00013.
- 958 [88] N. T. Carnevale and M. L. Hines, *The NEURON book*. Cambridge University
959 Press, 2006. DOI: 10.1017/CB09780511541612.
- 960 [89] R. A. McDougal, T. M. Morse, T. Carnevale, *et al.*, “Twenty years of ModelDB and
961 beyond: building essential modeling tools for the future of neuroscience,” *Journal*
962 *of Computational Neuroscience*, vol. 42, no. 1, 2017. DOI: 10.1007/s10827-016-
963 0623-7.
- 964 [90] R. Bestel, U. Van Rienen, C. Thielemann, and R. Appali, “Influence of Neuronal
965 Morphology on the Shape of Extracellular Recordings with Microelectrode Arrays:
966 A Finite Element Analysis,” *IEEE Transactions on Biomedical Engineering*,
967 vol. 68, no. 4, 2021. DOI: 10.1109/TBME.2020.3026635.
- 968 [91] M. Berggren and G. G. Malliaras, “How conducting polymer electrodes operate,”
969 *Science*, vol. 364, no. 6437, 2019. DOI: 10.1126/science.aaw9295.
- 970 [92] E. Syková and C. Nicholson, “Diffusion in brain extracellular space,” *Physiological*
971 *Reviews*, vol. 88, no. 4, 2008, ISSN: 00319333. DOI: 10.1152/physrev.00027.2007.
- 972 [93] J. R. Buitengeweg, W. L. Rutten, and E. Marani, “Modeled channel distributions
973 explain extracellular recordings from cultured neurons sealed to microelectrodes,”
974 *IEEE Transactions on Biomedical Engineering*, vol. 49, no. 12, pp. 1580–1590,
975 2002.
- 976 [94] M. Cucchi, D. Parker, E. Stavrinidou, P. Gkoupidenis, and H. Kleemann,
977 “In Liquido Computation with Electrochemical Transistors and Mixed Conductors
978 for Intelligent Bioelectronics,” *Advanced Materials*, 2023. DOI: 10.1002/adma.
979 202209516.

Supplementary material

Finite-element modeling of neuromodulation via controlled delivery of potassium ions using conductive polymer-coated microelectrodes

Claudio Verardo, Leandro Julian Mele, Luca Selmi, Pierpaolo Palestri

This file includes:

- Supplementary Tables S1-S5.
- Supplementary Figures S1-S12.
- Supplementary Note 1: COMSOL implementation details.
- Supplementary Note 2: model verification.
- Supplementary Note 3: reduced ionoCP-ECF model.

Table S1. Abbreviations used in the text.

Symbol	Description
FEM	Finite-element model
CP	Conductive polymer
isCP	Ideally-selective CP
nsCP	Non-selective CP
ionoCP	Ionophores-induced selective CP
PEDOT-PSS	poly(3,4-ethylenedioxythiophene) polystyrene sulfonate
OMIEC	Organic mixed ionic-electronic conductors
PNP	Poisson-Nernst-Planck
KNP	Kirchhoff-Nernst-Planck
ICF	Intracellular fluid
ECF	Extracellular fluid
AP	Action potential
HH	Hodgkin-Huxley
EDL	Electrical double layer
ORR	Oxygen reduction reactions
AMPA	α -amino-3-hydroxy-5-methyl-4-isoxazolepropionic receptor
EPSC	Excitatory postsynaptic current
WE	Working electrode
RE	Reference electrode
CE	Counter electrode
MEA	Multielectrode array

Table S2. Physical variables solved in the model (Figs. 1, 2 in the main body).

Symbol	Description	Domain of definition				Units
		ECF	ICF	Neural Membrane	CP	
ψ_c	electric potential (ions)	✓	✓		✓	mV
ψ_p	electric potential (holes)				✓	mV
$[K^+]$	K^+ concentration	✓	✓		✓	mM
$[Na^+]$	Na^+ concentration	✓	✓		✓	mM
$[Cl^-]$	Cl^- concentration	✓	✓		✓	mM
p	holes concentration				✓	mM
f_K	K^+ flux	✓	✓		✓	mol/(m ² s)
f_{Na}	Na^+ flux	✓	✓		✓	mol/(m ² s)
f_{Cl}	Cl^- flux	✓	✓		✓	mol/(m ² s)
f_p	holes flux				✓	mol/(m ² s)
V_{app}	potential applied to the PEDOT contact				✓	V
V	membrane potential			✓		mV
V_K	K^+ reversal potential			✓		mV
V_{Na}	Na^+ reversal potential			✓		mV
V_{Cl}	Cl^- reversal potential			✓		mV
$I_{K,DR}$	current K^+ voltage-gated channel			✓		$\mu A/cm^2$
$I_{Na,T}$	current Na^+ voltage-gated channel			✓		$\mu A/cm^2$
$I_{K,L}$	current K^+ leakage channel			✓		$\mu A/cm^2$
$I_{Na,L}$	current Na^+ leakage channel			✓		$\mu A/cm^2$
$I_{Cl,L}$	current Cl^- leakage channel			✓		$\mu A/cm^2$
I_K	total current K^+ channels			✓		$\mu A/cm^2$
I_{Na}	total current Na^+ channels			✓		$\mu A/cm^2$
I_{Cl}	total current Cl^- channels			✓		$\mu A/cm^2$
n	$I_{K,DR}$ activating gating variable			✓		-
m	$I_{Na,T}$ activating gating variable			✓		-
h	$I_{Na,T}$ inactivating gating variable			✓		-
[L]	concentration of free ionophores				✓	mM
[KL]	concentration of ionophores bound to K^+ ions				✓	mM
f_L	L flux				✓	mol/(m ² s)
f_{KL}	KL flux				✓	mol/(m ² s)
$I_{K,syn}$	K^+ current through AMPA synapse			✓		$\mu A/cm^2$
$I_{Na,syn}$	Na^+ current through AMPA synapse			✓		$\mu A/cm^2$

Table S3. Physical parameters and reference values used in the model (Figs. 1, 2 in the main body).

Symbol	Description	Value/expression			Units	Ref.
		ECF	ICF	CP		
T	temperature	309.15	309.15	309.15	K	[1]
RT/F	thermal voltage	26.64	26.64	26.64	mV	[1]
ϵ_{el}	cellular fluids dielectric constant	$80\epsilon_0$	$80\epsilon_0$	-	F/m	
ϵ_{PSS}	dielectric constant PSS phase	-	-	$80\epsilon_0$	F/m	
ϵ_{PEDOT}	dielectric constant PEDOT phase	-	-	$40\epsilon_0$	F/m	[2]
z_K	K^+ ion valence	+1	+1	+1	-	
z_{Na}	Na^+ ion valence	+1	+1	+1	-	
z_{Cl}	Cl^- ion valence	-1	-1	-1	-	
D_K	K^+ ion diffusivity	$2.19 \cdot 10^{-9}$	$2.19 \cdot 10^{-9}$	$5.08 \cdot 10^{-10}$	m^2/s	[3], [4]
D_{Na}	Na^+ ion diffusivity	$1.50 \cdot 10^{-9}$	$1.50 \cdot 10^{-9}$	$3.34 \cdot 10^{-10}$	m^2/s	[3], [4]
D_{Cl}	Cl^- ion diffusivity	$2.28 \cdot 10^{-9}$	$2.28 \cdot 10^{-9}$	$5.08 \cdot 10^{-10}$	m^2/s	[3], [4]
D_p	holes diffusivity	-	-	$D_p(p)^a$	m^2/s	[4]
$[K^+]_B$	K^+ bulk concentration	4	140	-	mM	[1]
$[Na^+]_B$	Na^+ bulk concentration	144	18	-	mM	[1]
$[Cl^-]_B$	Cl^- bulk concentration	130	6	-	mM	[1]
$[A^-]$	organic anion concentration	18^b	152^b	-	mM	
$[PSS^-]$	PSS fixed charges (polyanion)	-	-	Table S4	mM	[4]
C_V	volumetric capacitance	-	-	39	F/cm ³	[5]
B	Au-Ag/AgCl workfunction difference	-	-	-0.7	V	[4]
γ_K	CP-ECF virtual selectivity to K^+	-	-	1	-	
γ_{Na}	CP-ECF virtual selectivity to Na^+	-	-	Table S4	-	
γ_{Cl}	CP-ECF virtual selectivity to Cl^-	-	-	1	-	
L_D	Debye length	0.8^c	1.1^c	-	nm	[3]
z_L	L valence	-	-	0	-	
z_{KL}	KL valence	-	-	+1	-	
D_L	L diffusivity	-	-	$D_K/100$	m^2/s	
D_{KL}	KL diffusivity	-	-	$D_K/100$	m^2/s	
β_{KL}	association constant K^+ -L binding	-	-	100	1/M	
$k_{KL,b}$	backward rate constant K^+ -L binding	-	-	10^4	1/s	[6]
$k_{KL,f}$	forward rate constant K^+ -L binding	-	-	$k_{KL,b} \cdot \beta_{KL}$	1/(M s)	
$[L]_{tot}$	total concentration of L and KL	-	-	Table S4	mM	
Neural Membrane						
C_m	membrane capacitance	-	1	-	$\mu F/cm^2$	[1]
$\bar{g}_{K,DR}$	$I_{K,DR}$ max conductance	-	40	-	mS/cm ²	[1]
$\bar{g}_{Na,T}$	$I_{Na,T}$ max conductance	-	100	-	mS/cm ²	[1]
$\bar{g}_{K,L}$	$I_{K,L}$ conductance	-	0.05	-	mS/cm ²	[1]
$\bar{g}_{Na,L}$	$I_{Na,L}$ conductance	-	0.0175	-	mS/cm ²	[1]
$\bar{g}_{Cl,L}$	$I_{Cl,L}$ conductance	-	0.05	-	mS/cm ²	[1]
ϕ	temperature correction factor	-	3	-	-	[1]
α_n	n forward rate constant	-	$\frac{-0.01(V+34)\phi}{\exp(-0.1(V+34))-1}$	-	ms ⁻¹	[1]
β_n	n backward rate constant	-	$0.125\phi \exp(-\frac{V+44}{80})$	-	ms ⁻¹	[1]
α_m	m forward rate constant	-	$\frac{-0.1(V+30)\phi}{\exp(-0.1(V+30))-1}$	-	ms ⁻¹	[1]
β_m	m backward rate constant	-	$4\phi \exp(-\frac{V+55}{18})$	-	ms ⁻¹	[1]
α_h	h forward rate constant	-	$0.07\phi \exp(-\frac{V+44}{20})$	-	ms ⁻¹	[1]
β_h	h backward rate constant	-	$\frac{\phi}{\exp(-0.1(V+14))+1}$	-	ms ⁻¹	[1]
n_∞	n activation curve	-	$\frac{\alpha_n(V)}{\alpha_n(V)+\beta_n(V)}$	-	-	[1]
τ_n	n time constant	-	$\frac{1}{\alpha_n(V)+\beta_n(V)}$	-	ms	[1]
m_∞	m activation curve	-	$\frac{\alpha_m(V)}{\alpha_m(V)+\beta_m(V)}$	-	-	[1]
τ_m	m time constant	-	$\frac{1}{\alpha_m(V)+\beta_m(V)}$	-	ms	[1]
h_∞	h inactivation curve	-	$\frac{\alpha_h(V)}{\alpha_h(V)+\beta_h(V)}$	-	-	[1]
τ_h	h time constant	-	$\frac{1}{\alpha_h(V)+\beta_h(V)}$	-	ms	[1]
V_r	resting membrane potential	-	-67.0	-	mV	
$I_{K,r}$	current of K^+ channels at rest	-	$(I_{K,DR} + I_{K,L}) _{V=V_r} = 1.41$	-	$\mu A/cm^2$	
$I_{Na,r}$	current of Na^+ channels at rest	-	$(I_{Na,T} + I_{Na,L}) _{V=V_r} = -2.16$	-	$\mu A/cm^2$	
$I_{Cl,r}$	current of Cl^- channels at rest	-	$(I_{Cl,L}) _{V=V_r} = 0.75$	-	$\mu A/cm^2$	
$G_{Na,syn}$	Na^+ total conductance of AMPA synapse	-	2.22	-	nS	
$G_{K,syn}$	K^+ total conductance of AMPA synapse	-	4.90 ^d	-	nS	
$\bar{g}_{Na,syn}$	Na^+ conductance of AMPA synapse	-	$G_{Na,syn}/A_{neu} = 0.30$	-	mS/cm ²	
$\bar{g}_{K,syn}$	K^+ conductance of AMPA synapse	-	$G_{K,syn}/A_{neu} = 0.67$	-	mS/cm ²	
$\tau_{1,syn}$	slow time constant of AMPA synapse	-	3	-	ms	[7]
$\tau_{2,syn}$	fast time constant of AMPA synapse	-	1	-	ms	[7]

R gas constant, F Faraday constant, ϵ_0 vacuum dielectric constant.

^a $D_p(p) = 2.05 \cdot 10^{-5} (1.05 - 1.08 / (1 + \exp((p - 71.0) / 22.8)))$.

^b Set to provide electroneutrality in the bulk of ECF/ICS.

^c $L_D = \sqrt{\epsilon_{el} RT \cdot (F^2 \sum_i z_i^2 [X_i]_B)^{-1}}$ with $X_i \in \{K^+, Na^+, Cl^-\}$.

^d Set to have $I_{K,syn} = 0.5 |I_{Na,syn}|$ at $V = V_r$ as in [7].

Table S4. Parameters from Table S3 that are varied in order to instantiate the case studies considered in the main text (see Section 2.2): ideally-selective CP (isCP), non-selective CP (nsCP), ionophores-induced selective CP (ionoCP). We point out that $[L]_{\text{tot}} = 0$ corresponds to not including ionophores.

Symbol	Description	Value/expression			Units	Ref.
		isCP	nsCP	ionoCP		
γ_{Na}	CP-ECF virtual selectivity to Na^+	0	1	1	-	
$[L]_{\text{tot}}$	total concentration of L and KL	0	0	200	mM	
$[\text{PSS}^-]$	PSS fixed charges (polyanion)	2400	2400	637	mM	[4]

Table S5. Geometrical parameters and reference values used in this work (see Fig. 3).

Symbol	Description	Value	Units
W_{el}	electrolyte radius	40	μm
H_{el}	electrolyte height	40	μm
W_{p}	pillar radius	1.5	μm
H_{p}	pillar thickness	750	nm
d_{pm}	pillar-neuron cleft	50	nm
W_{CP}	CP length	15	μm
H_{CP}	CP thickness	600	nm
A_{CP}	CP surface area	905.9	μm^2
V_{CP}	CP volume	508.7	μm^3
d_{m}	membrane thickness	10	nm
d_{s}	sampling distance	6	nm
W_{neu}	neuron base radius	10	μm
H_{neu}	neuron height	4.5	μm
A_{neu}	neuron surface area	730.7	μm^2
V_{neu}	neuron volume	942.5	μm^3
d_{nn}	cleft between active and inactive neurons	541	nm
d_{CPm}	CP-neuron cleft	200	nm

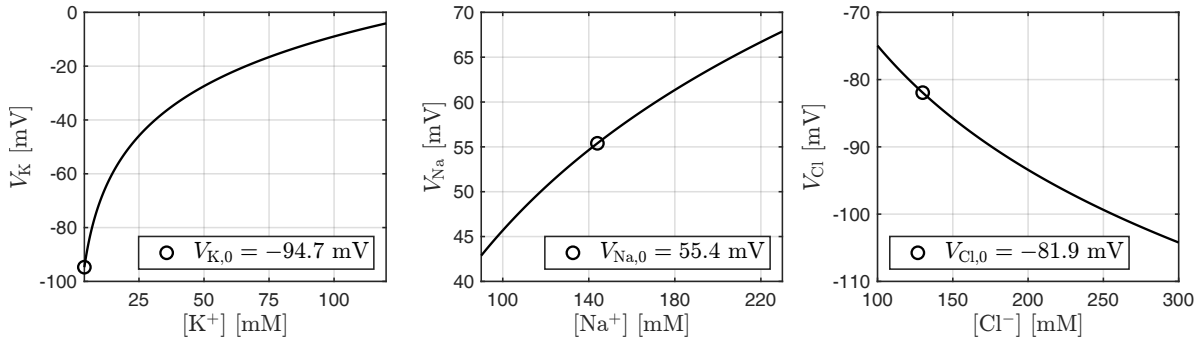


Figure S1. Reversal potentials V_{K} , V_{Na} , V_{Cl} evaluated in ranges of extracellular concentrations considered in the main text, according to the Nernst equation. The intracellular concentrations are kept to their baseline values (see Table S3). The baseline values for the reversal potentials are highlighted with circles. The potassium's reversal potential is the most sensitive to perturbation of the ionic milieu.

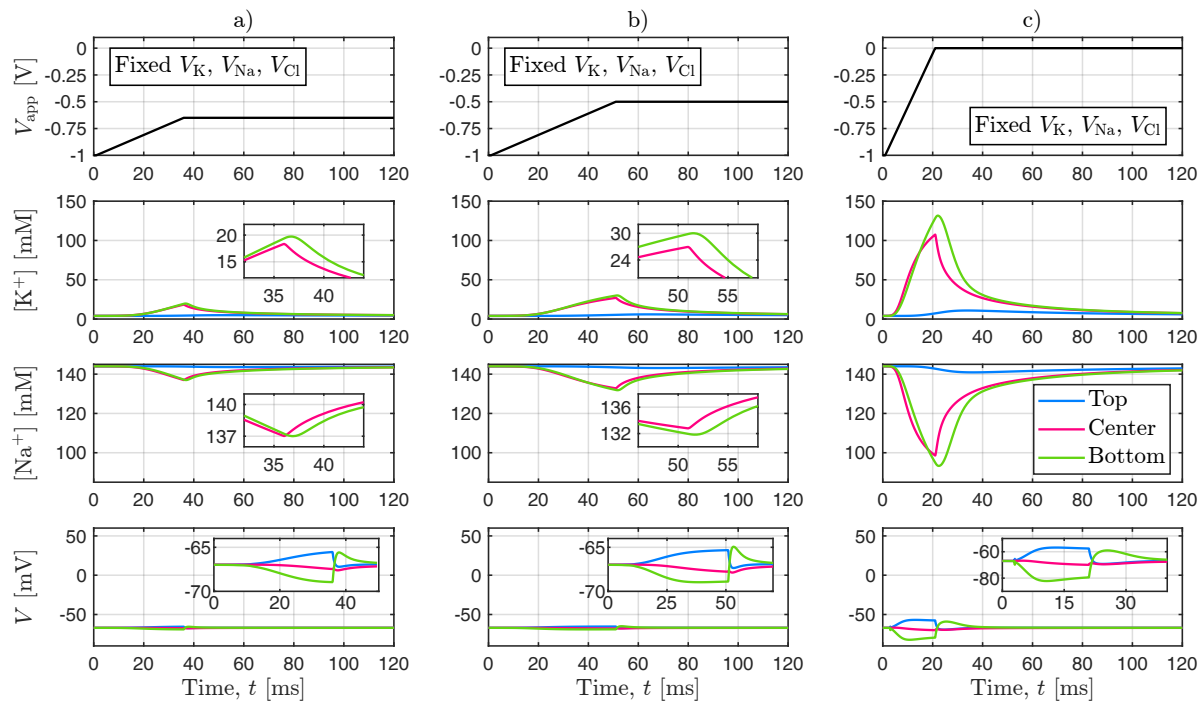


Figure S2. Ideally-selective CP (isCP). The same ionic stimulation transients of Fig. 4 are shown but with neuron reversal potentials fixed to their baseline values (see Fig. S1). Sanity check to confirm that the neural activity observed in Fig. 4 is mainly caused by the ionic component of neurostimulation (i.e., the released K^+). The hyperpolarization (respectively, depolarization) observed at the bottom (respectively, top) of the neuron are caused by the electric field induced in the ECF during ion release. The extents of such perturbations of membrane potential depend on the slope of the potential applied to the CP (compare columns a), b) with c)). From top to bottom, rows indicate: 1) the applied stimulus V_{app} , the extracellular concentrations of 2) $[K^+]$ and 3) $[Na^+]$ in different points of the ECF and 4) the membrane potential V .

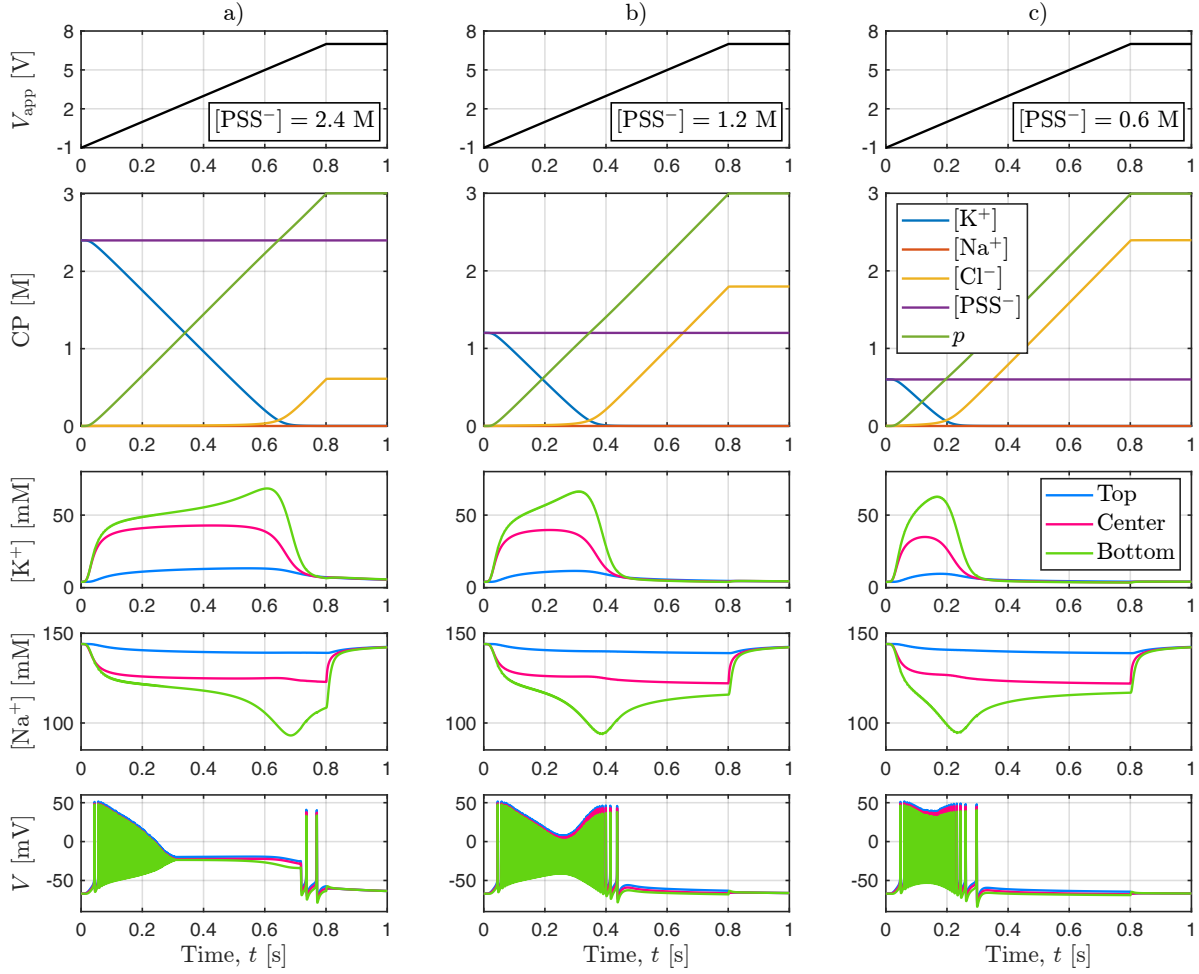


Figure S3. Ideally-selective CP (isCP). Examples of ionic stimulation performed with different concentrations of embedded fixed charges in the CP. a) $[\text{PSS}^-] = 2.4 \text{ M}$ (used as reference value as in the main text). b) $[\text{PSS}^-] = 1.2 \text{ M}$ (50% of the reference value). c) $[\text{PSS}^-] = 0.6 \text{ M}$ (25% of the reference value). Compared to Fig. 4, the ramps of applied potential are much longer ($v = 10 \text{ V/s}$ and $V_{\text{app,max}} = 7 \text{ V}$) in order to induce a complete depletion of potassium ions in the CP. We observe that higher concentrations of $[\text{PSS}^-]$ translate into longer time frames of K^+ release. From top to bottom, rows indicate: 1) the applied stimulus V_{app} , 2) the ion, hole and fixed charge concentrations inside the CP, the extracellular concentrations of 3) $[\text{K}^+]$ and 4) $[\text{Na}^+]$ in different points of the ECF, and 5) the membrane potential V . Interestingly, with such voltage ramp, larger than those used in the main body of the paper, the neuron response resembles seizure-like events (SLEs), with decreasing APs amplitudes and possible termination in configurations of depolarization block (see last row). The neuron recovers from such SLEs when all the K^+ stored in the CP has been released.

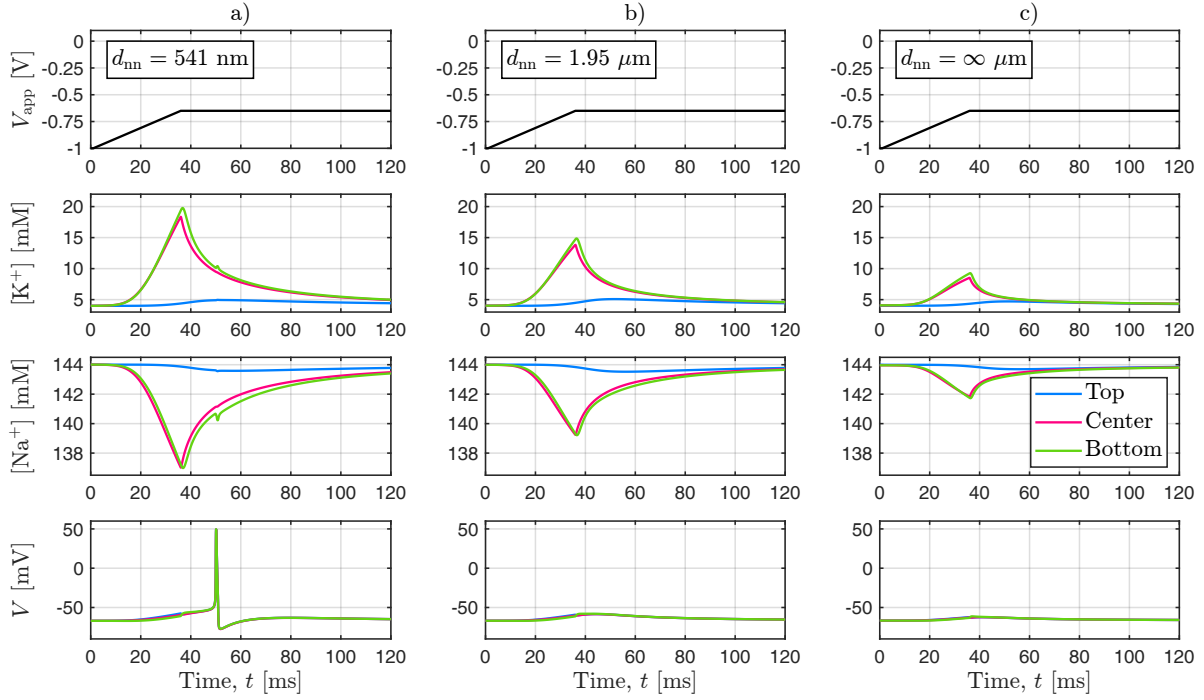


Figure S4. Ideally-selective CP (isCP). The ionic stimulation transient of Fig. 4.a is repeated for different extents of neuron’s lateral encumbrance. Namely, distances of the lateral inactive neurons d_{nn} (see Fig. 3): a) 541 nm (used as reference value in the main text), b) $1.95 \mu\text{m}$, and c) infinite (i.e., without lateral neurons). Configurations a), and b) correspond to geometries with neuronal area occupation of 90% and 70%, respectively. The area occupation is defined as the ratio between the 2D neuron area $A_{\text{neu}}^{2\text{D}} = \pi W_{\text{neu}}^2$ and the 2D area of its proximal extracellular microenvironment $A_{\mu\text{env}}^{2\text{D}} = \pi(W_{\text{neu}} + d_{nn})^2$, as seen from a top view. Larger occupations of area cause larger perturbations of the local ion concentrations in the ECF, for the same stimulation protocol. From top to bottom, rows indicate: 1) the applied stimulus V_{app} , the extracellular concentrations of 2) $[\text{K}^+]$ and 3) $[\text{Na}^+]$ in different points of the ECF, and 4) the membrane potential V .

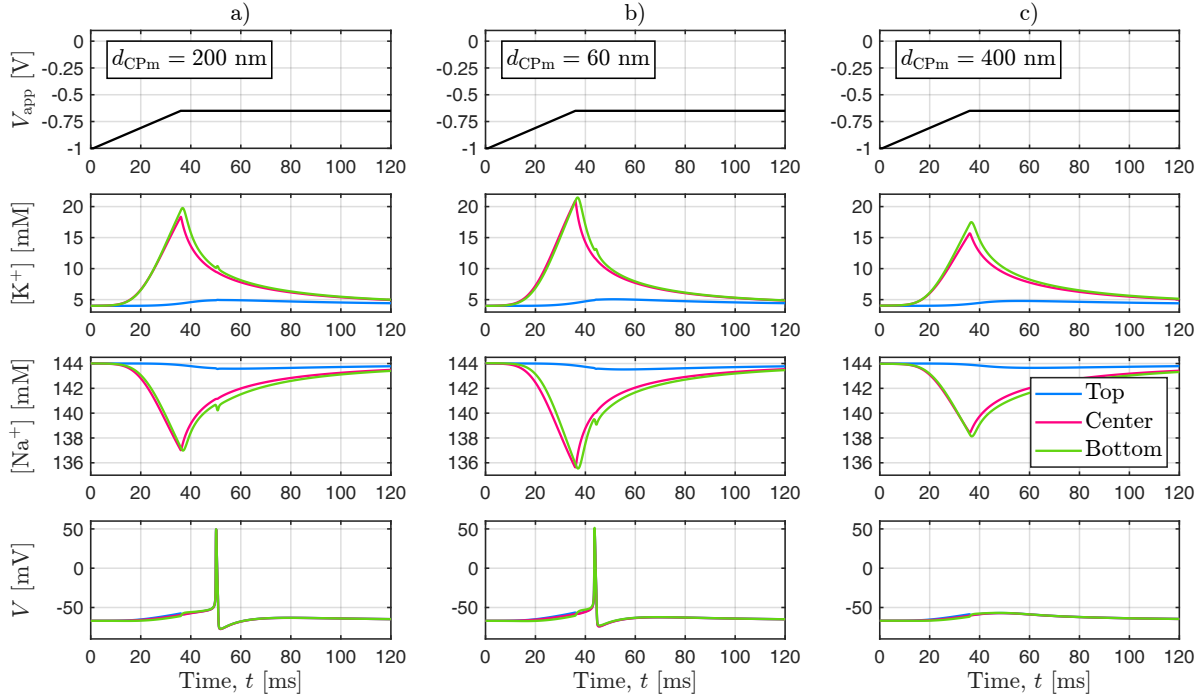


Figure S5. Ideally-selective CP (isCP). The ionic stimulation transient of Fig. 4.a is repeated for different extents of the CP-neuron cleft d_{CPm} (see Fig. 3): a) 200 nm (used as reference value as in the main text), b) 60 nm, and c) 400 nm. A smaller cleft yields a more pronounced perturbation of the local ion concentrations in the ECF, for the same stimulation protocol, which induces a larger depolarization of the neural membrane. The converse applies to a larger cleft. From top to bottom, rows indicate: 1) the applied stimulus V_{app} , the extracellular concentrations of 2) $[\text{K}^+]$ and 3) $[\text{Na}^+]$ in different points of the ECF, and 4) the membrane potential V .

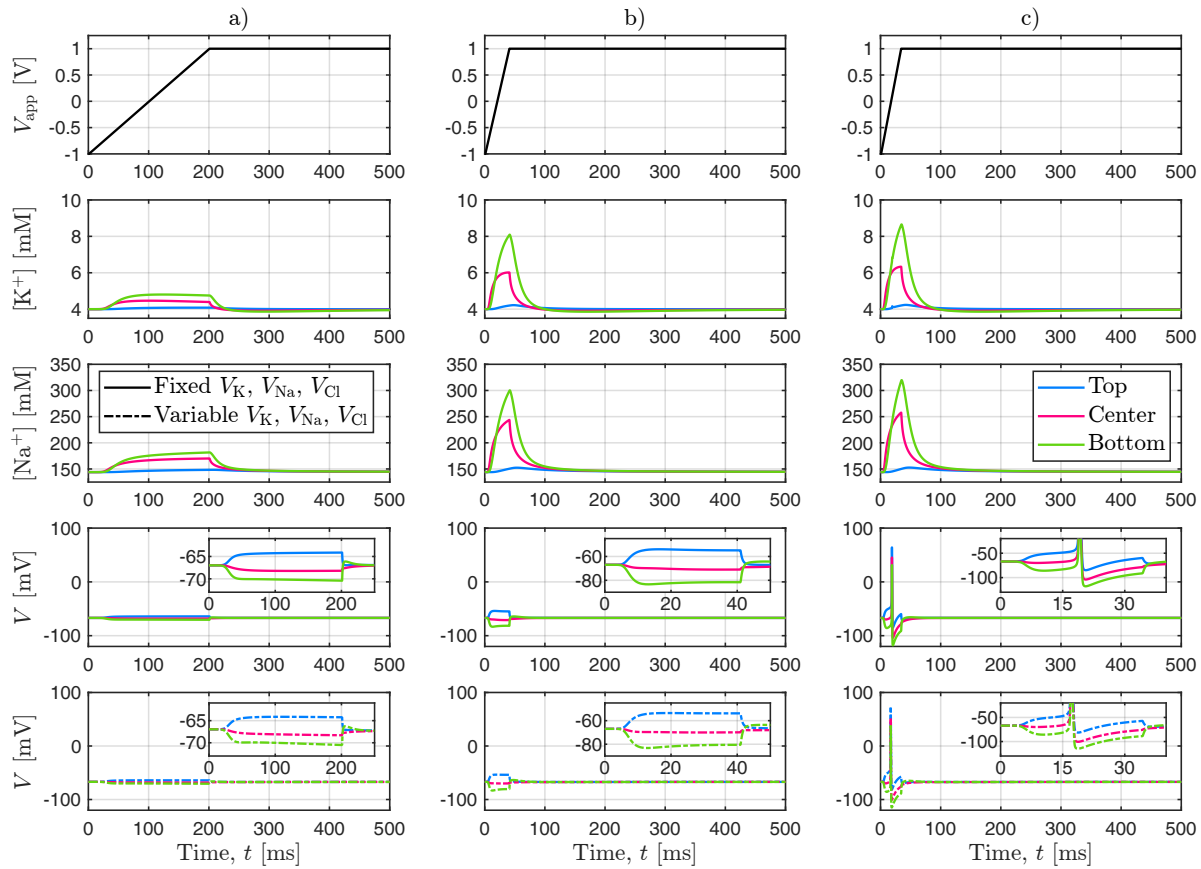


Figure S6. Non-selective CP (nsCP). Examples of ionic stimulation transients are performed by keeping either fixed or variable the reversal potentials V_K , V_{Na} , V_{Cl} . Different slopes of the applied potential are considered (with $V_{app,max} = 1$ V): a) $v = 10$ V/s (as in Fig. 6.b), b) $v = 50$ V/s, and c) $v = 60$ V/s (as in Fig. 6.c). This is a sanity check to confirm that the AP observed in Fig. 6 is mainly caused by the electric component of neurostimulation, rather than the change of the extracellular Na^+ and K^+ concentrations. From top to bottom, rows indicate: 1) the applied stimulus V_{app} , the extracellular concentrations of 2) $[K^+]$ and 3) $[Na^+]$ in different points of the ECF, and the membrane potential V setting 4) fixed or 5) variable reversal potentials during the simulation.

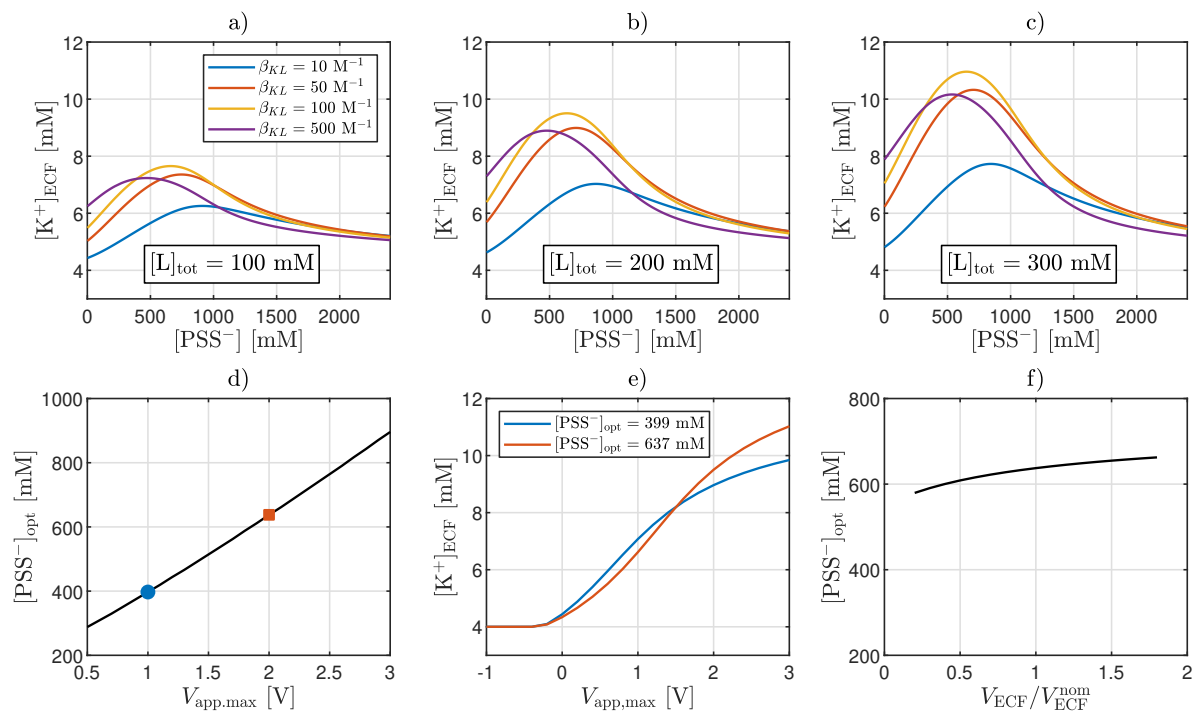


Figure S7. Optimizing the ionoCP properties with simulations based on a compartmentalized CP/ECF structure (see Supplementary Note 3). The optimum is evaluated based on the maximum $[K^+]$ change achievable in the ECF for $t \rightarrow +\infty$. a-c) K^+ vs fixed charge concentrations in the CP for different total concentrations of ionophore $[L]_{tot}$ in the polymer. While larger concentrations of ionophores yield larger release of K^+ , steric considerations suggest that an upper limit of ca. 200 mM. Interestingly, in all cases the optimum association constant is $\beta_{KL} = 100 M^{-1}$ (green curves). In this work, values as in (b) were used ($[PSS^-] \approx 637$ mM). Further analysis regarding the maximum voltage applied at the CP electrode, $V_{app,max}$, reveals that this parameter impacts the optimum amount of fixed charges (plot (d)). Plot (e) shows that changes of $[PSS^-]$ only slightly impact the ion actuation process, i.e., the change in $[K^+]$ in the extracellular cleft. (f) The choice of the ECF volume does not impact the optimum amount of fixed charges significantly (V_{ECF}^{nom} indicates the nominal value used in (a-e), see Supplementary Note 3).

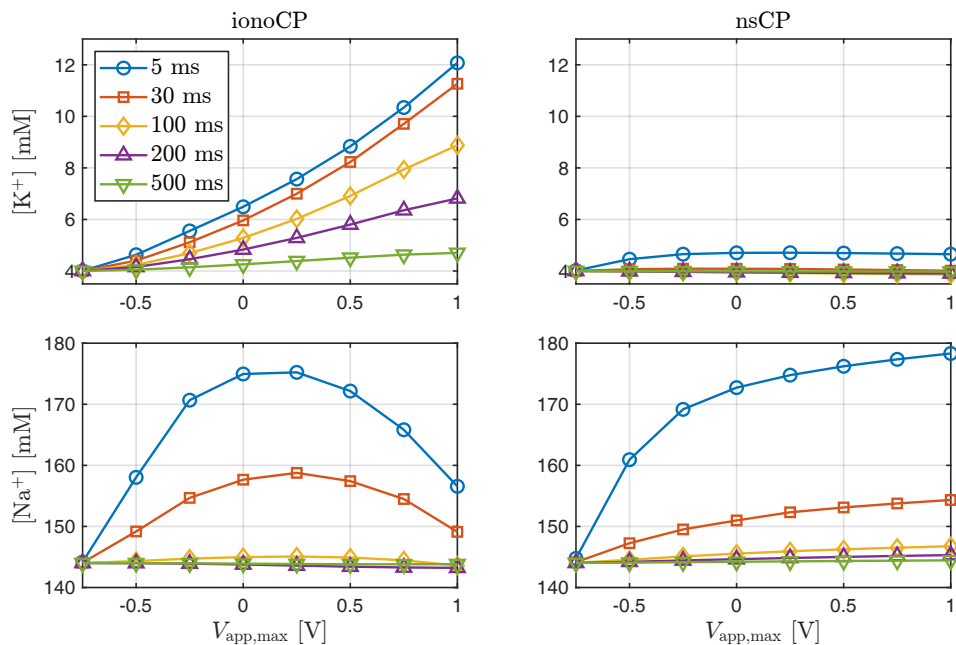


Figure S8. Comparison between (left) the ionophores-induced selective CP (ionoCP) and (right) the non-selective CP (nsCP). Simulations of ionic release are performed in both cases with a stimulus V_{app} with slope $v = 10$ V/s (as in Figs. 7.b and 6.b, respectively). Different values for the maximum applied potential $V_{app,max}$ are considered. From top to bottom, rows indicate: the concentrations of 1) K^+ and 2) Na^+ in the cleft between neuron and CP for different $V_{app,max}$ (markers) and different delays from the end of the V_{app} ramp (colors). The CP containing ionophores achieve higher $[K^+]$ modulation that persists in time due to the continuing unbinding processes of ionophores until a new equilibrium is reached. The modulation of $[Na^+]$ decays faster in both cases since associated only to sodium drift-diffusion in the ECF (similarly to K^+ in the nsCP case). Note that the ratio of the quantity of emitted K^+ and Na^+ increases with $V_{app,max}$ in the ionoCP case but not in the nsCP one. This means that the unbinding of ionophore complexes KL is promoted for larger potentials applied to the polymer.

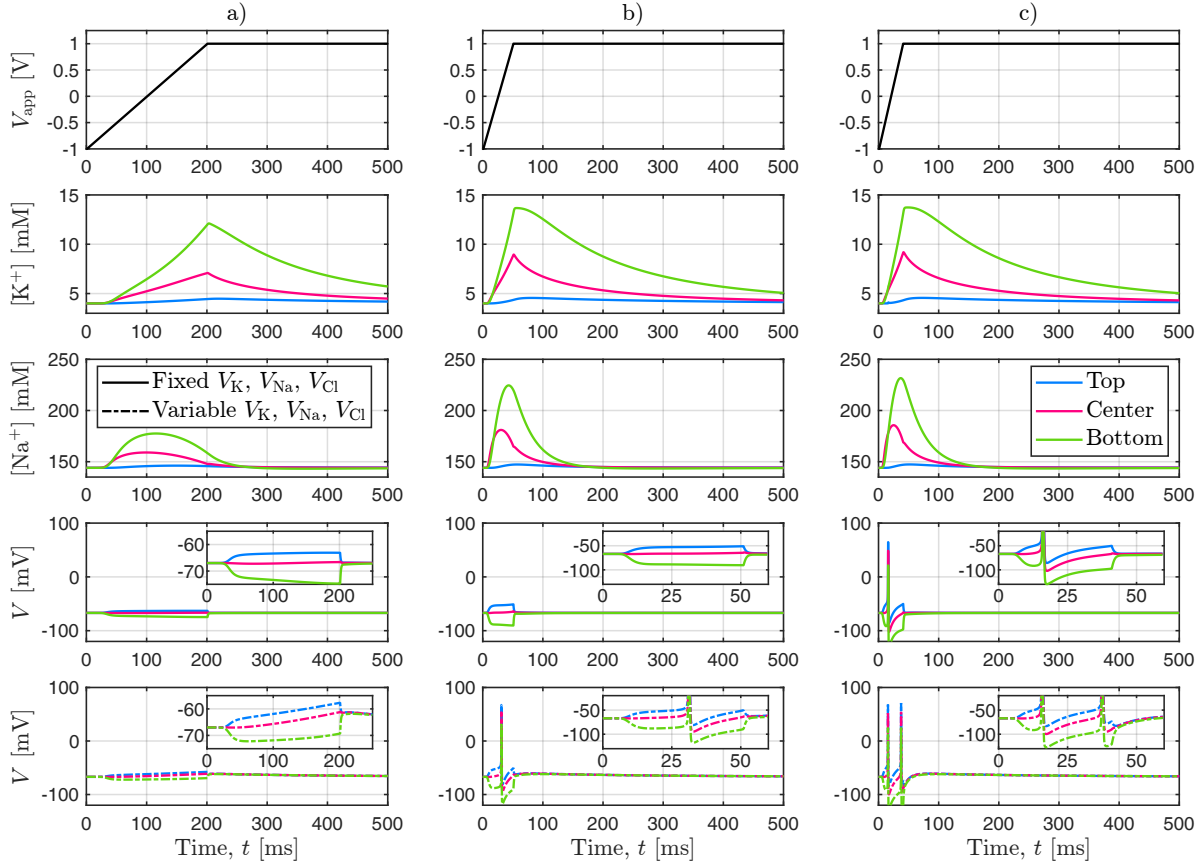


Figure S9. Ionophores-induced selective CP (ionoCP). Examples of ionic stimulation transients are performed by keeping either fixed or variable the neuron reversal potentials V_K , V_{Na} , V_{Cl} . Different slopes of the applied potential are considered (with $V_{app,max} = 1$ V): a) $v = 10$ V/s (as in Fig. 7.b), b) $v = 40$ V/s (as in Fig. 7.c), and c) $v = 50$ V/s. This is a sanity check to confirm that the AP observed in Fig. 7 results from both the electric and ionic components of neurostimulation. From top to bottom, rows indicate: 1) the applied stimulus V_{app} , the extracellular concentrations of 2) $[K^+]$ and 3) $[Na^+]$ in different points of the ECF, and the membrane potential V elicited with 4) fixed and 5) variable reversal potentials during the simulation.

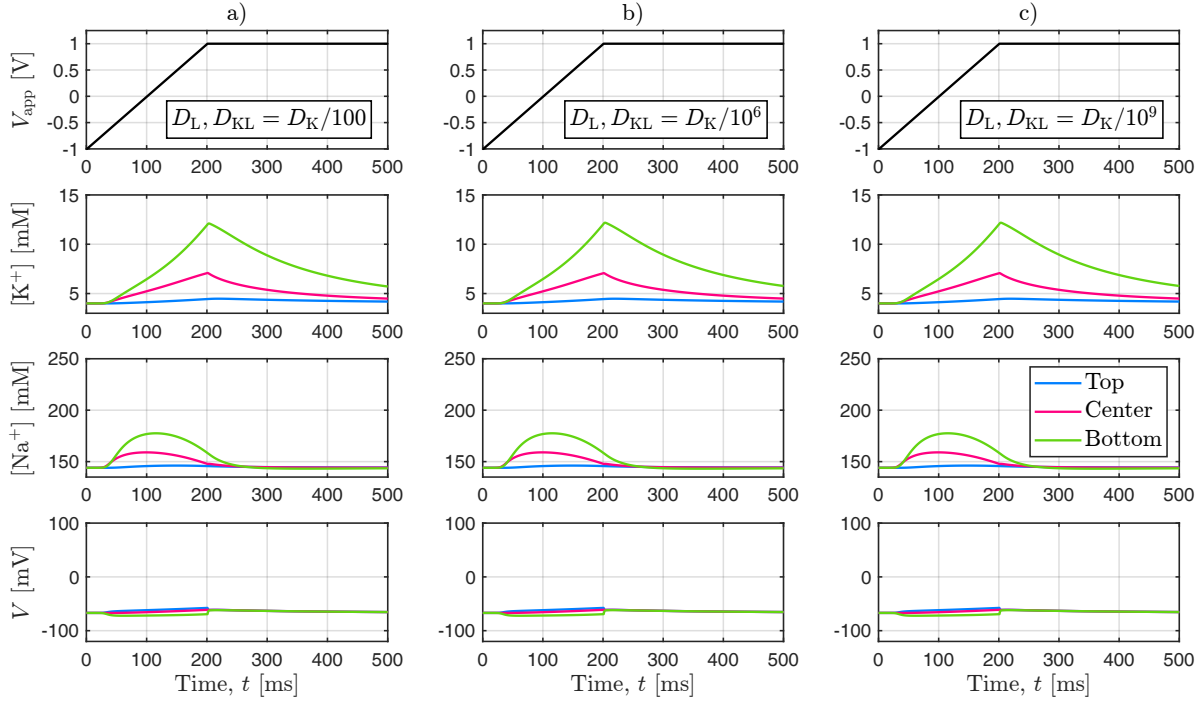


Figure S10. Ionophores-induced selective CP (ionoCP). The ionic stimulation transient of Fig. 9.b is shown for different values of the diffusivity coefficient of ionophores. Namely, by reducing them with respect to the one of free K^+ by a factor a) 100 (used as reference value as in the main text), b) 10^6 , and c) 10^9 (fixed ionophore approximation). The results are very mildly affected by this parameter, thereby confirming that the choice of modeling ionophores as mobile rather than fixed species is not critical. From top to bottom, rows indicate: 1) the applied stimulus V_{app} , the extracellular concentrations of 2) $[K^+]$ and 3) $[Na^+]$ in different points of the ECF, and 4) the membrane potential V .

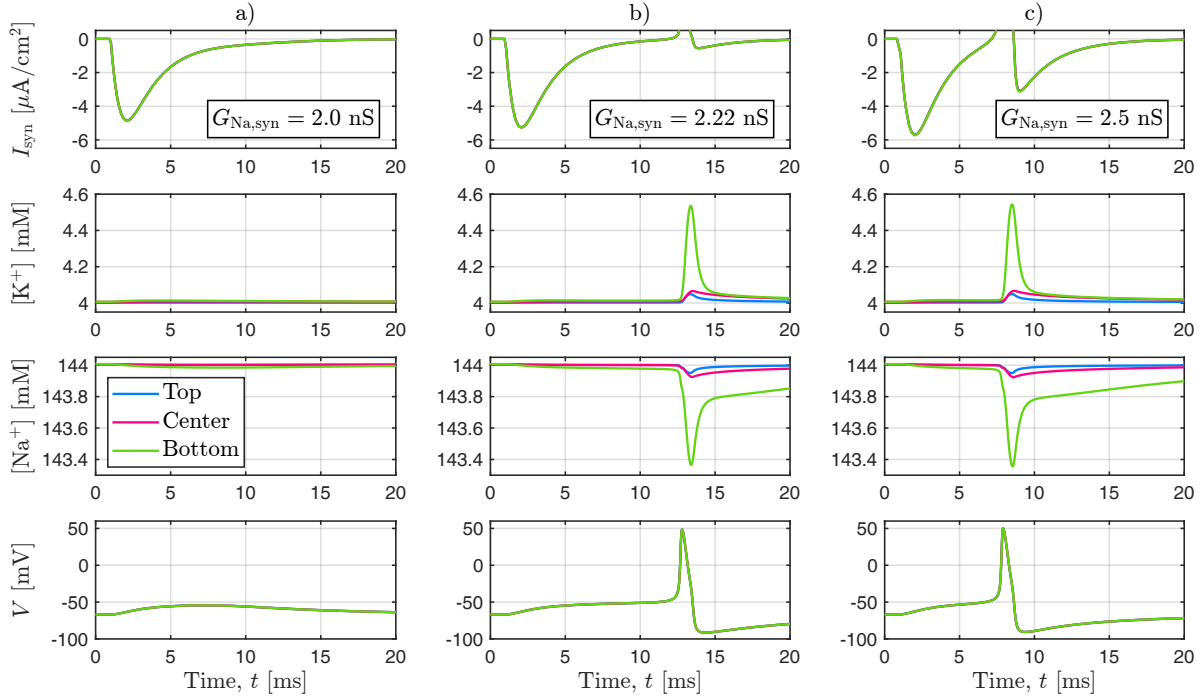


Figure S11. Calibration of the total synaptic conductance for sodium $G_{\text{Na},\text{syn}}$ to the threshold to elicit an AP. The potassium one $G_{\text{K},\text{syn}}$ is scaled accordingly (see footnote (d) in Table S3). Note that $G_{\text{Na},\text{syn}}$, $G_{\text{K},\text{syn}}$ are obtained by multiplying the synaptic conductances $g_{\text{Na},\text{syn}}$, $g_{\text{K},\text{syn}}$ mentioned in the main body by the neuronal surface area A_{neu} (see Table S5), and are adopted for ease of comparison with the original model of the synapse [7]. The CP, assumed ideal, is held at $V_{\text{app}} = -1$ V, hence no ionic release takes place. Three examples of synaptic events are shown for: a) a sub-threshold value $G_{\text{Na},\text{syn}} = 2.0$ nS (no AP elicited), b) the threshold value $G_{\text{Na},\text{syn}} = 2.22$ nS (AP elicited, used in the main body), and c) a supra-threshold value $G_{\text{Na},\text{syn}} = 2.5$ nS (AP elicited earlier than in (b)). The threshold has been found with an accuracy of the 2.2%. From top to bottom, rows indicate: 1) the total synaptic current $I_{\text{syn}} = I_{\text{K},\text{syn}} + I_{\text{Na},\text{syn}}$, the extracellular concentrations of 2) $[\text{K}^+]$ and 3) $[\text{Na}^+]$ in different points of the ECF, and 4) the membrane potential V .

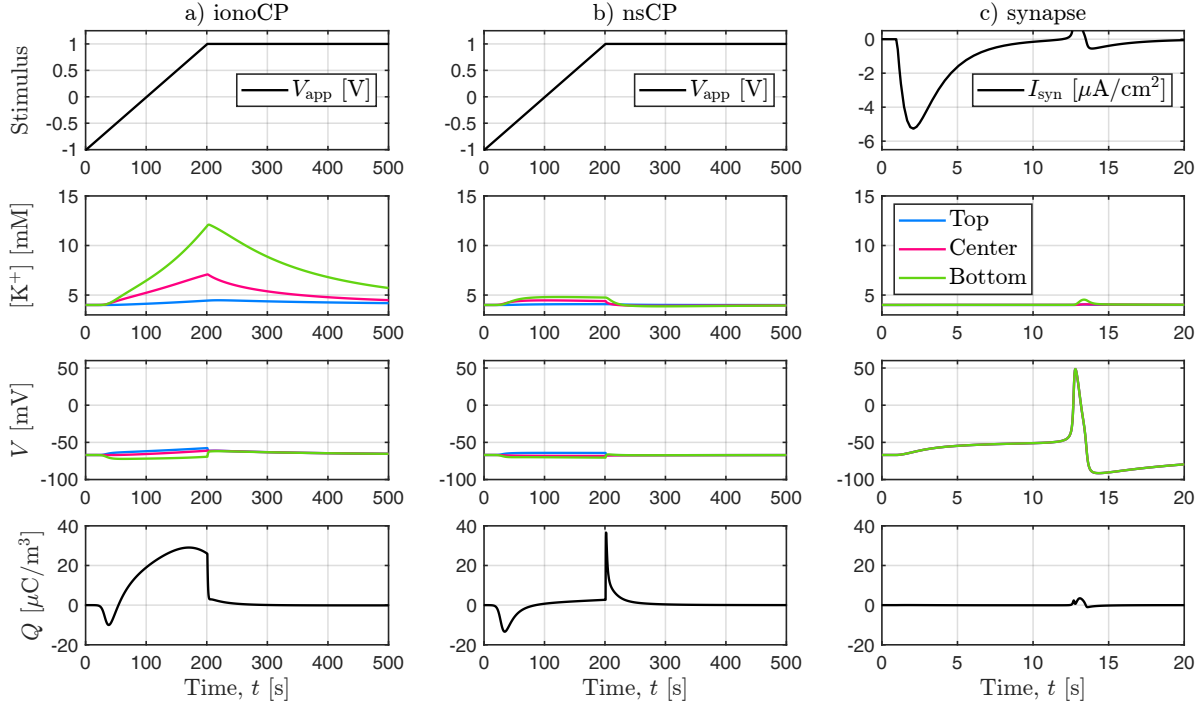


Figure S12. Test of electroneutrality in the CP-neuron cleft. Two transients of ionic stimulation are considered for a) the ionophores-induced selective CP (ionoCP) and b) the non-selective CP (nsCP). They are compared to the purely physiological case of synaptic-induced AP in c). We point out that the transients a)-c) correspond to those in Fig. 7.b, Fig. 6.b, and Fig. S11.b, respectively. From top to bottom, rows indicate: 1) the applied stimulus (either the potential applied to the CP, V_{app} , or the synaptic current, I_{syn}), 2) the extracellular concentration of $[\text{K}^+]$, 3) the membrane potential V , and 4) the deviation of charged ionic species from electroneutrality in the CP-neuron cleft $Q = F([\text{K}^+] + [\text{Na}^+] - [\text{Cl}^-] - [\text{A}^-])$. The charge induced in a) results up to an order of magnitude greater than that in c). The charge in b) is instead comparable to that in c), with the exception of the starting and ending phases of the V_{app} ramp. We also point out that the time scales in a)-b) are much larger than in c), with charge density perturbation lasting hundreds of ms in the former ones while just a few ms in the latter one. These results suggest that the electroneutrality assumption might not be trivially satisfied in the ionoCP case. Only more in-depth investigations and comparisons with the KNP formalism (see Discussion) can better shed light on the problem.

Supplementary Note 1: COMSOL implementation details

The model equations reported in Figs. 1, 2 of the main body were implemented using COMSOL Multiphysics v6.0 [8]. For the sake of reproducibility, we herein report the main features adopted in our models.

Rotational symmetry To enforce the symmetry around the vertical axis of the geometry (see Fig. 3), the model has been implemented as a *2D Axisymmetric Component*. In such a way, the 3D geometry is defined by its 2D cross-section, and the model equations are automatically adapted to ensure rotational symmetry in the solutions.

Physical interfaces PNP models employed for the ICF, ECF and CP were obtained by combining the *Transport of Dilute Species* and *Electrostatic* physical interfaces, that belong to the electrochemistry and AC/DC packages, respectively. Given the peculiar form of the PNP model describing the CP (see Fig. 1 in the main text), we used user-defined variables to handle the coupling between Poisson and continuity equations, instead of the built-in multiphysics features. The HH model was implemented using *Boundary Ordinary Differential Equations (Boundary ODEs)* at the neuron membrane boundaries. Sample points at 6 nm distance inside and outside the cell membrane were made accessible to the HH model for computing the reversal potentials by using *linear extrusion* operators, available among non-local coupling functions. Similar functions were also employed to create a common set of variables at both sides of the membrane boundary.

Meshing Meshes were designed using the non-linear *Boundary Layer* mesh-generator with an initial element size of subnanometer length (set using the minimum step size allowed by COMSOL) close to charged interfaces, followed by mesh elements whose size varies exponentially until a maximum predefined size is reached. The number of mesh elements along boundaries was controlled by the *distribution* feature. In the bulk of each simulation domain, the maximum predefined size was set to 1.5 μm in the ECF, 0.6 μm in the ICF, and 0.15 μm in the CP. A convergence analysis was performed to make sure that the selected mesh size provided sufficient accuracy on the results. As shown in Figure S13, a reduction of the maximum element size in the chosen mesh does not induce any change in the solution found by the model.

Studies The initial conditions for ionic actuation transients in the isCP and nsCP cases were found through stationary studies. In the ionoCP case, to help convergence, the initial conditions were found via a stationary study with the dynamics of ionophores disabled and followed by a time-dependent study (10 s) of the full model. Ionic actuation transients starting from such initial conditions were simulated through time-dependent studies with *intermediate* time step setting. The results shown in the main text were sampled at the actual time steps taken by the solver using *probes*.

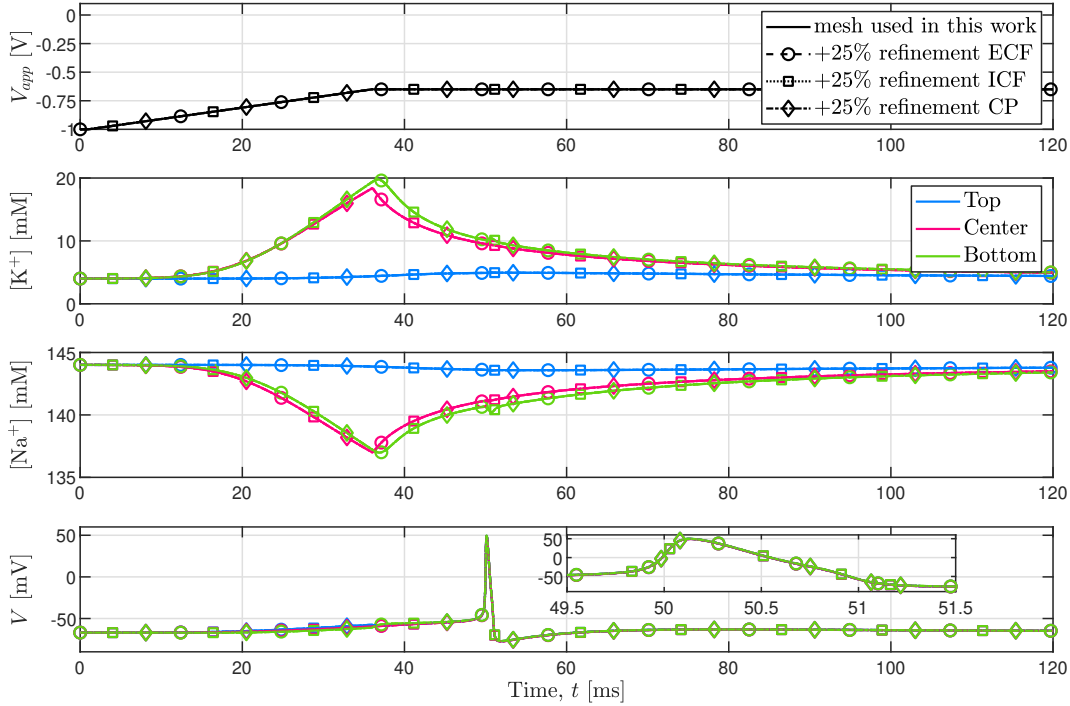


Figure S13. Convergence analysis of the mesh used in the work. The transient in Fig. 4.a (here, in solid lines) is repeated after reduction of the 25% of the maximum element size in the ECF (dashed lines), ICF (dotted line), and CP (dashed-dotted line). From top to bottom, rows indicate: 1) the applied stimulus to the CP V_{app} , the extracellular concentration of 2) $[K^+]$ and 3) $[Na^+]$, and 4) the membrane potential V . The results are in perfect agreement (all curves overlap), thereby confirming the appropriate meshing of the system.

Computational burden Given the numerical complexity of the modeled problems, we used a cluster of servers to perform simulations. To this aim, we employed the *batch* command-line interface to COMSOL Multiphysics.

To provide a glimpse on the mentioned computational burden, we herein report the computational time for the parameter sweeps in Figs. 9.B and 9.D. For such simulations, two servers with the following specifications were used in parallel:

- Server 1: 2x Intel® Xeon® CPU X5690 at 3.47 GHz (12 cores), 189 GB RAM.
- Server 2: 2x Intel® Xeon® CPU Gold 6136 at 3.00 GHz (24 cores), 500 GB RAM.

Simulations in Fig. 9.B consisted of time-dependent studies lasting 300 ms with a maximum time step of 1 ms. The total solving time was 30:53:03 (hh:mm:ss), with 13:52:22 carried out by Server 1 and 17:00:41 by Server 2. Table S6 reports the times (mm:ss) of each simulation (bold text: Server 1, plain text: Server 2).

Simulations in Fig. 9.D consisted of time-dependent studies lasting 400 ms with a maximum time step of 1 ms. The total solving time was 39:03:26 (hh:mm:ss), with 19:32:55 carried out by Server 1 and 19:30:31 by Server 2. Table S7 reports the times (mm:ss) of each simulation (bold text: Server 1, plain text: Server 2).

Table S6. Simulation time of the studies in Fig. 9.B.

		$V_{\text{app,max}}$ [V]							
		-0.75	-0.50	-0.25	0	0.25	0.50	0.75	1.00
scale $g_{X_i,\text{syn}}$	0.9	32:37	45:54	44:46	23:52	24:50	24:12	24:18	24:20
	0.8	32:35	35:20	45:57	23:56	23:36	23:46	23:47	24:02
	0.7	31:31	33:56	33:43	23:36	24:07	24:29	24:45	24:22
	0.6	33:21	34:14	34:11	18:16	24:36	24:34	24:23	24:08
	0.5	31:30	34:42	33:50	18:00	18:08	24:29	24:07	23:49
	0.4	32:09	34:00	33:01	18:19	17:52	18:53	23:51	24:24
	0.3	32:00	34:04	18:07	17:45	17:48	18:09	18:24	24:28
	0.2	31:12	33:50	17:59	17:34	18:00	18:16	18:22	18:27
	0.1	31:21	32:38	18:06	17:53	17:33	17:57	17:56	18:10

Table S7. Simulation time of the studies in Fig. 9.D.

		$V_{\text{app,max}}$ [V]							
		-0.75	-0.50	-0.25	0	0.25	0.50	0.75	1.00
scale $g_{X_i,\text{syn}}$	0.9	41:54	44:57	55:55	28:23	28:39	29:12	29:18	29:25
	0.8	42:04	43:57	44:23	28:41	28:08	29:31	29:43	29:01
	0.7	42:08	44:33	43:27	29:30	29:15	29:53	28:56	28:52
	0.6	42:35	43:49	43:19	23:33	23:12	30:30	28:24	30:13
	0.5	41:37	43:47	43:28	23:25	23:04	23:56	29:45	29:11
	0.4	41:44	44:12	43:54	22:39	23:23	23:31	23:05	29:52
	0.3	41:16	43:28	43:10	23:21	22:25	23:21	23:32	23:35
	0.2	41:04	43:02	43:20	23:16	22:25	23:11	23:31	23:30
	0.1	41:29	42:04	42:19	22:52	22:48	23:03	22:37	22:54

Supplementary Note 2: model verification

Given the transient nature of the mechanisms under study, we are interested in time-dependent simulations of the polymer – cellular fluids – neural membrane system (see Fig. 1 in the main text). To the extent of our knowledge, analytical solutions are not available for such scenarios. Therefore, to verify the correct implementation of our model, we considered simplified geometries and limit cases as benchmarks.

Simplified geometry: AP propagation along an unmyelinated fiber We reproduced the results of electrodiffusive model for an unmyelinated axon (1 μm diameter, 10 mm length) from [9]. Therein, the system was implemented with a formalism very similar to ours (the minor differences are discussed in Sections 2.1.2 - 2.1.3) and solved with a custom software. Figure S14.a shows that our COMSOL implementation reproduces quite closely the propagation of an action potential excited by a 0.965 nA stimulus applied at $t = 0$ for 2 ms (namely, Fig. 2 in [9]). The propagation velocity results 0.90 ms/s instead of 0.93 m/s as in [9]. Notwithstanding, the referenced work does not provide a convergence analysis of the solution. The difference emerges from the finer mesh employed in our model, with a minimum element size of 0.07 μm along the transverse direction (instead of 0.5 μm in [9]) and 5 μm along the longitudinal direction (instead of 100 μm in [9]). Indeed, as shown in Fig. S14.b, we find a better agreement by simulating the system with a coarser mesh resembling that of [9]. This analysis confirms the correctness of our implementation of the coupling between the neural membrane and the cellular fluids.

Limit case: ohmic approximation for cellular fluids A verification of the entire system (including the conductive polymer) has been carried out considering the limit case of electrical stimulation. This limit case occurs when the perturbation of ionic concentrations in the extracellular fluid during the actuation phase is negligible, and the electric field increase is the main mechanism responsible for generating the action potential. In this case (referred to as *pure electrical stimulation* in the main text), the electrolyte can be effectively modeled as an ohmic conductor, thereby neglecting diffusion currents. This formalism is typically employed to model the interface between neurons and implanted electrodes, both for stimulation [10] and recording [11].

In the ohmic electrolyte approximated model, the PNP equations (Eqs. 1-3 in Fig. 1) are replaced in our COMSOL deck by

$$\nabla \cdot \left(\sigma_{\text{el}} \nabla \psi_c + \varepsilon_{\text{el}} \frac{\partial \nabla \psi_c}{\partial t} \right) = 0, \quad (\text{S1})$$

where σ_{el} is the ionic conductivity, defined as

$$\sigma_{\text{el}} = \frac{F^2}{RT} (D_{\text{K}} [\text{K}^+]_{\text{B}} + D_{\text{Na}} [\text{Na}^+]_{\text{B}} + D_{\text{Cl}} [\text{Cl}^-]_{\text{B}}). \quad (\text{S2})$$

By inserting the parameters values used in Table S3 we obtain $\sigma_{\text{el}} = 1.3 \text{ S/m}$ for the extracellular fluid and $\sigma_{\text{el}} = 2.0 \text{ S/m}$ for the intracellular fluid. While the description of

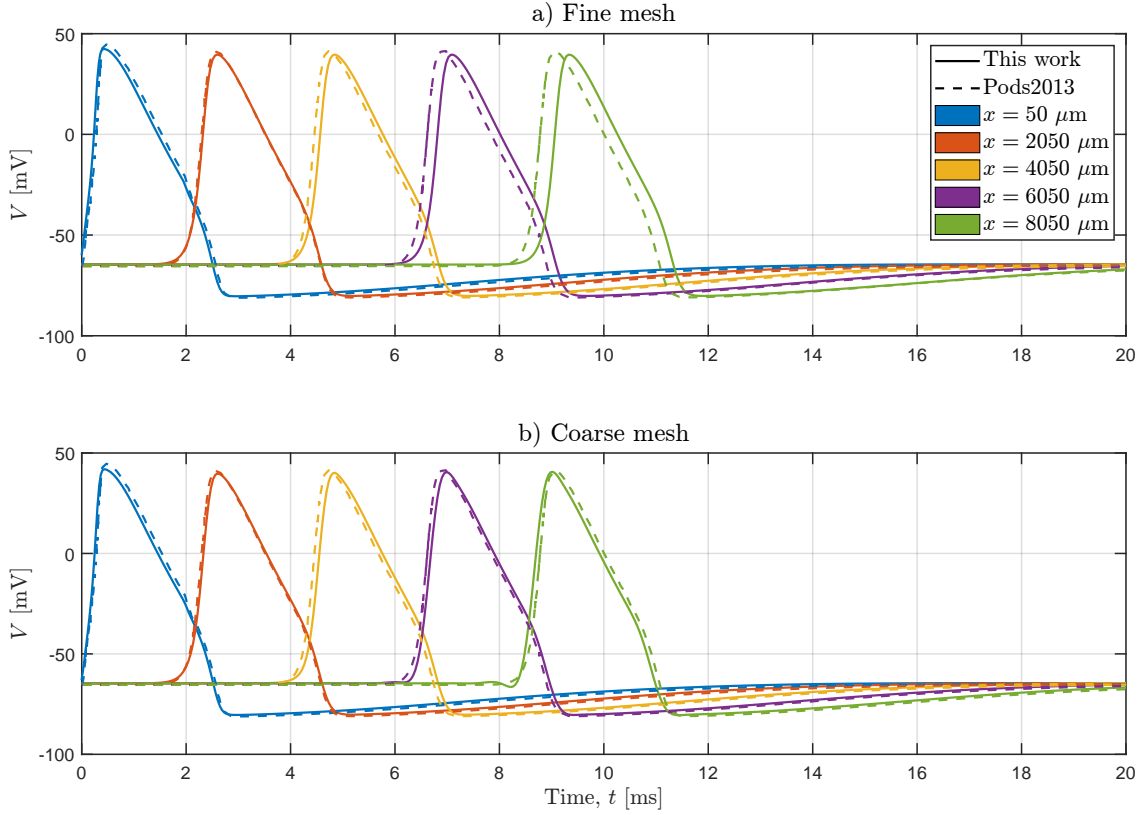


Figure S14. Comparison of our model to the electrodiffusive model of unmyelinated axon from [9]. The system is excited by a 0.965 nA stimulus applied at $t = 0$ for 2 ms. The solid lines represent the membrane potential predicted by our model, while the dashed ones are from Fig. 2 in [9]. The x refers to the longitudinal position along the axon where the membrane potential V is sampled. In a) we use a finer mesh than in [9]. In b) we use a coarser mesh resembling the one used in [9].

the neural membrane (HH model) does not change (Eqs. 6-8 in Fig. 1), the boundary conditions that couple the neural membrane and the cellular fluids (Eqs. 4-5, 9-10 in Fig. 1) need to be substituted with

$$\hat{u} \cdot \nabla \psi_c \Big|_{\text{extra}}^{\text{intra}} = \mp \left(C_m \frac{dV}{dt} + I_K + I_{\text{Na}} + I_{\text{Cl}} \right), \quad (\text{S3})$$

$$V = \psi_c \Big|_{\text{intra}} - \psi_c \Big|_{\text{extra}}, \quad (\text{S4})$$

where \hat{u} is the vector normal to the membrane surface. In a similar way, the conductive polymer is substituted by a flux boundary condition that injects in the extracellular fluid the same ionic current predicted by the electrodiffusive model (i.e., the PNP model in COMSOL) according to

$$\hat{u} \cdot (\sigma_{\text{el}} \nabla \psi_c) \Big|_{\text{CP}} = I_{\text{CP}} = F \frac{d}{dt} \left(\int_{\text{CP}} p \, d\Omega \right). \quad (\text{S5})$$

Figure S15 reports the ionic actuation transients obtained with the non-selective CP (nsCP) following either the electrodiffusive or the ohmic formalisms. Two widths of the

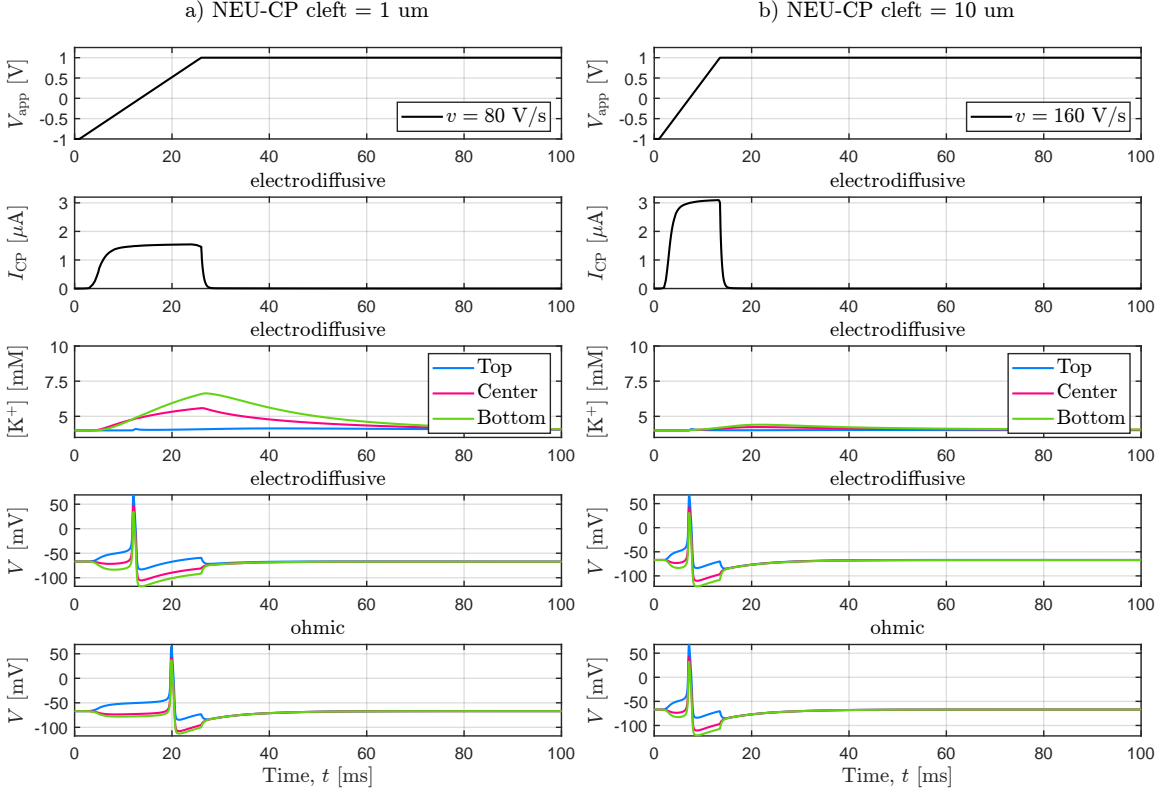


Figure S15. Comparison of the predictions of the electrodiffusive and ohmic models during an actuation transient with the non-selective CP (nsCP). The title of each inset denotes the model used to solve the plotted variable. In a) a neuron-CP cleft of 1 μm is considered and the two model predictions differ due to the non-negligible change of ionic concentrations. Conversely, in b) a neuron-CP cleft of 10 μm is considered and the results of the two models are in good mutual agreement.

neuron-CP cleft (d_{CP_n}) are considered: a) 1 μm and b) 10 μm . The rows 1-4 of the plots are results from simulations of the electrodiffusive model, while row 5 contains the results from the ohmic model. In a), the perturbation of ionic concentrations is not negligible due to the small size of the neuron-CP cleft. Therefore, the profile of membrane potential predicted by the two models differs. In fact, in this situation, the electrodiffusive description is more general than the ohmic one. In b) the cleft is very large and ionic concentrations are mildly perturbed by the action of the ionic actuator. Therefore, the predictions of the two models are in good agreement, corroborating the correctness of the implementation of our electrodiffusive model (that naturally tends to the ohmic model in the cases where this latter is valid).

Supplementary Note 3: reduced ionoCP-ECF model

For the optimization of the ionophores-induced selective CP (ionoCP), we considered a phase-boundary model of the interaction between the ionic actuator and the ECF. Namely, we lumped the CP, CP contact, and ECF in compartments. Further, we considered only the equilibrium state of the system. The model is employed to study, 1), the precharging capacity of the ionoCP and, 2), the subsequent release step (see Section 3.3 and Fig. S7).

ionoCP precharge: This model assumes:

- (i) Electroneutrality everywhere in the domain.
- (ii) Electrodiffusion processes at thermodynamic equilibrium. Namely, concentrations follow Boltzmann distributions

$$[X_i] = [X_i]_B \left(-\frac{z_{X_i} F}{RT} \exp(\psi_c - \psi_{c,B}) \right) \quad (S6)$$

$$p = p_M \left(-\frac{F}{RT} \exp(\psi_p - \psi_{p,M}) \right), \quad (S7)$$

where $X_i \in \{K^+, Na^+, Cl^-\}$. The subscript B denotes the reference point for ionic concentrations and is taken at the bulk of the ECF. The subscript M denotes the reference point for holes and is taken at the CP (metal) contact.

- (iii) Chemical reactions (for ionophores) are at thermodynamic equilibrium, i.e., it holds

$$\beta_{KL} = \frac{[KL]}{[K^+]_{CP}[L]} \quad (S8)$$

- (iv) Mass conservation for ionophores:

$$[L] + [KL] = [L]_{tot} \quad (S9)$$

We point out that (ii) and (iii) hold true at equilibrium only if ionophores are regarded as fixed species, i.e., their fluxes f_L , f_{KL} are null. As seen in the main body, this is not a critical assumption. Hereafter, we summarize the variables solved in the reduced model and those set according to assumption i) ‡.

Full model	Reduced model			Units
	CP contact	CP	ECF	
ψ_c	-	ψ_c	$\psi_{c,B} = 0$	V
ψ_p	$\psi_{p,M} = -1$	ψ_p	-	V
$[K^+]$	-	$[K^+]_{CP}$	$[K^+]_B = 4$	mM
$[Na^+]$	-	$[Na^+]_{CP}$	$[Na^+]_B = 144$	mM
$[Cl^-]$	-	$[Cl^-]_{CP}$	$[Cl^-]_B = 130$	mM
$[L]$	-	$[L]$	-	mM
$[KL]$	-	$[KL]$	-	mM
p	$p_M = 97.97$	p	-	M

‡ p_M assumed from the concentration of free electrons in gold, i.e., $5.9 \cdot 10^{28} \text{ m}^{-3}$.

In the model equations considered in this study there are 8 free variables to solve: ψ_c , ψ_p , $[K^+]_{CP}$, $[Na^+]_{CP}$, $[Cl^-]_{CP}$, $[L]$, $[KL]$, p . From the assumptions i), ii), iii), and iv) follow the below Eqs. S5.a-b), c-f), g), and h), respectively.

$$[K^+]_{CP} + [Na^+]_{CP} - [Cl^-]_{CP} + p - [PSS^-] + [KL] = 0 \quad (S10a)$$

$$p - \frac{C_V}{F}(\psi_p - \psi_c) = 0 \quad (S10b)$$

$$[K^+]_{CP} - [K^+]_B \exp\left(-\frac{F\psi_c}{RT}\right) = 0 \quad (S10c)$$

$$[Na^+]_{CP} - [Na^+]_B \exp\left(-\frac{F\psi_c}{RT}\right) = 0 \quad (S10d)$$

$$[Cl^-]_{CP} - [Cl^-]_B \exp\left(\frac{F\psi_c}{RT}\right) = 0 \quad (S10e)$$

$$p - p_M \exp\left(\frac{F}{RT}(V_{app,0} - \psi_p)\right) = 0 \quad (S10f)$$

$$[KL] - \beta_{KL}[K^+]_{CP}[L] = 0 \quad (S10g)$$

$$[L] + [KL] - [L]_{tot} = 0 \quad (S10h)$$

ionoCP release: this study analyzes the concentration change of potassium ions in the ECF at equilibrium based on the final value of the applied stimulus at the metal contact, $\psi_{p,M} = V_{app,max}$. Therefore, the model uses the solution obtained with the pre-charging study (see above) as initial conditions for concentrations of potassium ions (free and complexed indicated as $[K^+]_{CP,0}$ and $[LK]_0$ in the following) and enforces mass conservation of these ions using fixed CP and ECF volumes. This model has therefore 9 unknown variables to solve: the 8 of the previous study plus $[K^+]_{ECF}$:

$$[K^+]_{CP} + [Na^+]_{CP} - [Cl^-]_{CP} + p - [PSS^-] + [KL] = 0 \quad (S11a)$$

$$p - \frac{C_V}{F}(\psi_p - \psi_c) = 0 \quad (S11b)$$

$$[K^+]_{CP} - [K^+] \exp\left(-\frac{F\psi_c}{RT}\right) = 0 \quad (S11c)$$

$$[Na^+]_{CP} - [Na^+]_B \exp\left(-\frac{F\psi_c}{RT}\right) = 0 \quad (S11d)$$

$$[Cl^-]_{CP} - [Cl^-]_B \exp\left(\frac{F\psi_c}{RT}\right) = 0 \quad (S11e)$$

$$p - p_M \exp\left(\frac{F}{RT}(V_{app,max} - \psi_p)\right) = 0 \quad (S11f)$$

$$[KL] - \beta_{KL}[K^+]_{CP}[L] = 0 \quad (S11g)$$

$$[L] + [KL] - [L]_{tot} = 0 \quad (S11h)$$

$$([K^+]_{CP} + [LK] - [K^+]_{CP,0} - [LK]_0)V_{CP} + ([K^+] - [K^+]_B)V_{ECF} = 0, \quad (S11i)$$

where V_{CP} and V_{ECF} are the volumes of the CP and the ECF, respectively.

Compartments volume: while V_{CP} is given by the adopted geometry (see Table S5), the value used for V_{ECF} must reflect the dynamics of the ionic actuator, namely the

ion diffusion space around the CP for a given time interval. In fact, this optimization tool provides an estimate on the total modulation at $t = \infty$ while the ionoCP operates in dynamic conditions. Thus, one way to exploit the results of the simplified model is to assume an effective volume that is actually modulated during the ion release, before ions disperse in the bulk of ECF. In this paper, based on the results presented in the main body, we used an interval $\Delta t = 150$ ms and considered the ECF volume as the 3D space within $\sqrt{D_K \Delta t}$ all around the CP, and subtracted the volume occupied by the neuron cell.

Solver: Solutions of Eqs. (S10) and (S11) were found developing an *ad-hoc* Newton-Raphson solver. Parameters such as β_{KL} , $[PSS^-]$, $[L]_{tot}$, $V_{app,max}$ were varied according to the optimization process as described in the main body.

References

- [1] J. R. Cressman, G. Ullah, J. Ziburkus, S. J. Schiff, and E. Barreto, “The influence of sodium and potassium dynamics on excitability, seizures, and the stability of persistent states: I. single neuron dynamics,” *Journal of computational neuroscience*, vol. 26, no. 2, pp. 159–170, 2009. DOI: 10.1007/s10827-008-0132-4.
- [2] M. O. Bamgbopa, J. Edberg, I. Engquist, M. Berggren, and K. Tybrandt, “Understanding the characteristics of conducting polymer-redox biopolymer supercapacitors,” *Journal of Materials Chemistry A*, vol. 7, no. 41, pp. 23 973–23 980, 2019. DOI: 10.1039/c9ta07030c.
- [3] A. J. Bard, L. R. Faulkner, and H. S. White, *Electrochemical methods: fundamentals and applications*, 2nd ed. John Wiley & Sons Inc., 2001, ISBN: 9780471043720.
- [4] K. Tybrandt, I. V. Zozoulenko, and M. Berggren, “Chemical potential–electric double layer coupling in conjugated polymer–polyelectrolyte blends,” *Science advances*, vol. 3, no. 12, eaao3659, 2017. DOI: 10.1126/sciadv.aao3659.
- [5] J. Rivnay, P. Leleux, M. Ferro, *et al.*, “High-performance transistors for bioelectronics through tuning of channel thickness,” *Science Advances*, vol. 1, no. 4, pp. 1–6, 2015. DOI: 10.1126/sciadv.1400251.
- [6] J. J. Jasielec, T. Sokalski, R. Filipek, and A. Lewenstam, “Neutral-Carrier Ion-Selective Electrodes Assessed by the Nernst-Planck-Poisson Model,” *Analytical Chemistry*, vol. 87, no. 17, 2015. DOI: 10.1021/acs.analchem.5b00065.
- [7] M. J. Sætra, G. T. Einevoll, and G. Haldnes, “An electrodiffusive neuron-extracellular-glia model for exploring the genesis of slow potentials in the brain,” *PLoS Computational Biology*, vol. 17, no. 7, 2021. DOI: 10.1371/journal.pcbi.1008143.
- [8] *Comsol multiphysics user manual*, COMSOL Inc., Sweden, 2022.
- [9] J. Pods, J. Schönke, and P. Bastian, “Electrodiffusion models of neurons and extracellular space using the poisson-nernst-planck equations - Numerical simulation of the intra- and extracellular potential for an axon model,” *Biophysical Journal*, vol. 105, no. 1, 2013. DOI: 10.1016/j.bpj.2013.05.041.
- [10] A. Fellner, A. Heshmat, P. Werginz, and F. Rattay, “A finite element method framework to model extracellular neural stimulation,” *Journal of Neural Engineering*, vol. 19, no. 2, p. 022 001, Apr. 2022. DOI: 10.1088/1741-2552/AC6060.
- [11] R. Bestel, U. Van Rienen, C. Thielemann, and R. Appali, “Influence of Neuronal Morphology on the Shape of Extracellular Recordings with Microelectrode Arrays: A Finite Element Analysis,” *IEEE Transactions on Biomedical Engineering*, vol. 68, no. 4, 2021. DOI: 10.1109/TBME.2020.3026635.